

SAND2015-XXXXR

LDRD PROJECT NUMBER: 173655

LDRD PROJECT TITLE: Fully Coupled Simulation of Lithium Ion Battery Cell Performance

PROJECT TEAM MEMBERS: Bradley L. Trembacki, Jayathi Y. Murthy, and Scott A. Roberts

ABSTRACT:

Lithium-ion battery particle-scale (non-porous electrode) simulations applied to resolved electrode geometries predict localized phenomena and can lead to better informed decisions on electrode design and manufacturing. This work develops and implements a fully-coupled finite volume methodology for the simulation of the electrochemical equations in a lithium-ion battery cell. The model implementation is used to investigate 3D battery electrode architectures that offer potential energy density and power density improvements over traditional layer-by-layer particle bed battery geometries. Advancement of micro-scale additive manufacturing techniques has made it possible to fabricate these 3D electrode microarchitectures. A variety of 3D battery electrode geometries are simulated and compared across various battery discharge rates and length scales in order to quantify performance trends and investigate geometrical factors that improve battery performance. The energy density and power density of the 3D battery microstructures are compared in several ways, including a uniform surface area to volume ratio comparison as well as a comparison requiring a minimum manufacturable feature size. Significant performance improvements over traditional particle bed electrode designs are observed, and electrode microarchitectures derived from minimal surfaces are shown to be superior. A reduced-order volume-averaged porous electrode theory formulation for these unique 3D batteries is also developed, allowing simulations on the full-battery scale. Electrode concentration gradients are modeled using the diffusion length method, and results for plate and cylinder electrode geometries are compared to particle-scale simulation results. Additionally, effective diffusion lengths that minimize error with respect to particle-scale results for gyroid and Schwarz P electrode microstructures are determined.

INTRODUCTION:

Motivation and Battery Background

Research in lithium-ion batteries has proliferated during the last decade as a result of their recognition as a viable green alternative to energy transport and storage [1] [2]. Though well-developed for portable electronics applications, there are numerous challenges to be overcome for their use in heavy duty applications like electric vehicles or grid storage [3] [4] [5] [6] [7]. Modeling and simulation of these battery systems play a critical role in their effective and safe commercialization for such high energy density applications [8] [9] [10].

A typical lithium-ion battery consists of a porous composite anode and cathode filled with an electrolyte and separated by a porous separator [11]. Both the anode and cathode electrodes are composed of spatially dispersed active particles of lithium insertion compounds (LiCoO_2 , LiMn_2O_4 , LiFePO_4 , graphite, coke etc.), forming particle beds. These solid (non-porous) particles are held together by a binder, resulting in the formation of a porous structure. The electrolyte resides in the pores wetting the active particle bed, providing a high electrode/electrolyte interfacial surface area [12]. In addition, additives like carbon are also dispersed throughout to enhance certain desired properties such as electrical conductivity [13] [14]. The anode-separator-cathode stack percolated with electrolyte is sandwiched between two current collectors, the whole assembly often called a cell sandwich. This architecture facilitates the shuttling of lithium ions between anode and cathode through the electrolyte while forcing the flow of electrons through the external circuit, thus delivering power. On a cell level, experimentalists are continuously trying to maximize the performance of batteries by varying the shapes and sizes of the active particles, material volume fractions, etc. [15] [16] [17] [18] [19]. Simulation of batteries with realistic electrode architectures would tremendously help guide these experiments.

The spatial concentration of the lithium ions and electric potential gradients govern the transport of species and charge throughout the battery. By imposing conservation principles, governing equations for species and charge transport applicable for various phases (electrodes, electrolytes) are derived [20]. Charge transfer kinetics at the electrode-electrolyte interface are governed by the Butler-Volmer equations [20]. Solutions of the species and charge transport equations with proper boundary and interfacial conditions yield the spatial and temporal distribution of concentration and electric potential fields in the different phases, information that is difficult or impossible to obtain experimentally. Furthermore, this information can be used to characterize the performance of batteries using metrics like energy density and power density.

Volume-Averaged Modeling and Simulation

To simulate electrochemical behavior of batteries on a cell level, volume-averaged models (porous electrode theory) are widely used [20] [21] [22] [23] [24]. Volume averaging involves homogenization of the various phases of the porous electrode, eliminating the need to resolve the electrode microstructure [25]. The governing equations are averaged over a representative elementary volume (REV) that contains both electrolyte and electrode phases. Such an REV is large compared to a particle size, but small compared to the overall battery cell size. Since the interface between phases is no longer represented, the interfacial reactions described in the previous section are averaged over the entire REV and act as volumetric source/sink terms for each material. Instead of the intrinsic properties of the various constituents, these models employ effective transport properties that are analytically derived based on various geometric simplifications such as uniformly sized spherical active material particles [14]. Volume-averaging a cell sandwich effectively reduces the equations to be one-dimensional, since the only direction of transport is between the current collectors on either end of the battery. This reduction in dimensionality makes full-battery simulations in a reasonable timeframe possible.

Butler-Volmer kinetics govern ion transport between electrode and electrolyte, and therefore overall discharge performance. Therefore, these simplified volume-averaged models were improved by more accurately representing interface values of species and potential, which directly dictate the Butler-Volmer current density. Originally, the porous electrode theory developed by Newman and Tiedemann assumed that the interface concentrations were constants [26]. However, that assumption represents an equilibrium state, and a charging/discharging battery is not in equilibrium. This becomes especially important when considering solid phase (electrode) lithium diffusion. Doyle et al. improve the porous electrode theory by incorporating solid diffusion limitations. They consider diffusion in a spherical particle at each point in the homogenized domain. By assuming radially symmetric diffusive behavior with the radial direction being the primary diffusion direction, they create a pseudo-2D system of equations that captures solid diffusion limitations. While an improvement on the more simplistic porous electrode theory, solving a 2D system is significantly more computationally complex than the original 1D formulation. Rather than solve the full 2D system, they solve the radial transport in a spherical particle numerically using Duhamel's superposition method along with the 1D volume-averaged equations [22] [27]. This method provides significant improvement in computation time when compared to solving the 2D system; however, it is limited to the assumptions of a simple particle shape (sphere, cylinder, etc.) and constant mass diffusivity. Wang et al. offer an alternative approach that can be termed the diffusion length method where the concentration profile is assumed to be parabolic, thus providing a simple linear relationship between the volume-averaged concentration and the concentration at the electrode surface. This method is not limited to any particular particle shape, and the effective diffusion length reflects the underlying morphology [28]. Effective diffusion lengths corresponding to spherical, cylindrical, and plate-like particles were analytically derived. While not as precise as the superposition method employed by Doyle et al., it provides a more generic simplistic system that is still effectively 1D and is shown to be sufficient under most battery operating conditions. An empirical correction factor was introduced to the diffusion length method to produce results that more closely resemble the superposition method [29]. Over time, several alternative approaches to capturing solid diffusion within a volume-averaged simulation, such as polynomial approximation and sub-grid methods, have been published [30] [31]. Other variables of interest at the interface, such as electrolyte concentration and electric potential in both the electrode and electrolyte are typically assumed to be equivalent to their volume-averaged values due to their higher relative transport characteristics compared to solid phase diffusion and therefore insignificant gradients.

The previous work on volume-averaged battery simulation discussed here assumes that there are three distinct regions in the battery: an anode region, a separator region, and a cathode region. Anode/cathode equations are presented in a generic electrode format, since there are no points in the battery where an REV contains both anode and cathode. This is due to the inherently layer-by-layer design of traditional particle bed batteries, and may not be applicable for other electrode geometries where an REV contains non-porous particles/structures of both anode and cathode. To our knowledge, no such reformulation has been developed as such 3D microbatteries are just now being manufactured and researched as discussed below in the *3D Batteries* subsection.

Particle-Scale Simulations

It is well known that actual electrode microstructure can be different from the idealizations discussed above [32]. It is therefore necessary to develop models that more closely represent the actual three-dimensional geometry, fully resolving the various phases (active material, carbon, binder, electrolyte) of the electrode. Until recently, it was not possible to obtain the real 3D geometry of the battery microstructure. This is being made possible with the advent of instruments like Micro-Computed Tomography (μ CT) scanners, which have been used to characterize sintered porous materials including lithium-ion battery electrodes [33] [34] [35]. Additionally, Focused Ion Beam-Scanning Electron Microscopes (FIB-SEM) in conjunction with advanced image processing techniques have been used to successfully capture and recreate microstructures [36] [37] [38] [39] [40]. These techniques are commonly used to characterize 3D microstructures for a variety of applications such as solid oxide fuel cells and lithium-ion batteries. The reconstructed geometry obtained from these methods can provide detailed information about active particle shape and size, which can be used to generate more realistic synthetic computational geometries that are not limited to spherical particle shapes. Furthermore, through the use of specialized software, the reconstructed geometries can be converted directly into a finite volume/element mesh for numerical simulations [41] [14]. Performing transport simulations on these fully resolved synthetic and real geometries, explicitly partitioned into various constituent phases, can be termed as particle-scale or pore-scale modeling [42] [43] [44] [45] [46]. Full scale simulations of this type at the cell level would allow for better comparison with experiments. Furthermore, particle-scale simulations performed on representative elemental volumes can be used to develop multi-scale constitutive models resulting in more accurate volume-averaged transport models [14]. There is therefore a significant interest in the battery community in such particle-scale simulations.

Goldin et al. [42] performed a fully resolved particle scale simulation on a synthetic full cell sphere-packed geometry, where the particle bed is modeled as intersecting spheres. By varying the radius, packing arrangement, and the overlap of the spheres, they emulated various electrode microstructures. The simulations were used to evaluate the effective transport properties commonly used for volume-averaged models. The electrochemical model was solved using a sequential method where each equation is solved consecutively until convergence has been reached and was performed using the commercial software ANSYS Fluent. Wiedemann et al. extended the simulation effort by applying the same sequential algorithm to real particle bed cathode microstructure meshes [43], evaluating the effects of geometry on battery performance. For computational simplicity, the concentration and the potential field were determined only in the fully resolved cathode; these variables were assumed constant throughout the electrolyte phase. Less et al. [44] solved the electrochemical equations for a fully resolved cathode microstructure based on particle size distribution information gathered from FIB-SEM scans using the finite volume framework in a fully-coupled solution procedure. Apart from these two methods, Orvananos et al. solved the fully resolved model using a meshless method called the smoothed boundary method [47].

Additionally, some recent work applying electrochemistry directly to real particle bed reconstructions has been published. Within the Aria framework at Sandia National Laboratories, Roberts et al. developed an automated method for creating a finite element mesh from 2D FIB-

SEM image stacks and focus on simulating the swelling and mechanical deformation processes that occur during electrode lithiation [48]. Hutzenlaub et al. reconstructed their real bed FIB-SEM scans previously cited and were able to identify carbon binder in addition to active material and electrolyte material, which is the simpler image processing approach that others have taken. The reconstruction was adapted into a 21-million cell hexahedral mesh and an electrochemical simulation was performed at a 1C discharge rate. Their simulation was performed inside the commercial software platform STAR-CCM+, and they report a simulation time of 27 days using 8 CPUs [49]. As the sizes of the meshes employed for numerical simulations corresponding to real electrode geometries are enormously high (on the order of 10⁸ cells or above), these simulations can easily span weeks. A fully implicit and fast solution of the electrochemical model is needed in order to conduct a sufficient number of electrochemical simulations on a range of electrode sample reconstructions. Additionally, creating high-quality finite volume meshes from the reconstructed geometries is a significant technical challenge, and developing a process to create such meshes in a straightforward and consistent process is required before widespread simulations can be performed.

3D Batteries

While characterizing and simulating common commercial electrode particle bed microstructures as previously discussed is an important pursuit, there is also growing interest in the battery community in developing electrode configurations that differ significantly from particle beds. The manufacturing process of a traditional battery consists of milling large areas of anode particle bed slurry, porous electrolyte separator, and cathode particle bed slurry [50]. This layer-by-layer approach generates a battery design where all ions must traverse a significant distance to move from one electrode to the other.

Electrode configurations that have the potential to improve battery performance using interpenetrating configurations that shorten ion path lengths have been proposed [51]. In addition to improved performance, microbatteries using such configurations offer an alternative to capacitors as microchip power and energy sources [51]. Recent advancements in micro-scale additive manufacturing techniques have made it possible to fabricate complex geometries at micron-scale feature sizes [52] [53]. There has been recent interest in using these techniques to print active electrode materials and fabricate microbatteries that were previously only theoretical. Lewis et al. printed several alternating-plate 3D interpenetrating lithium-ion batteries using a functional ink direct write process with a resolution of 30 μm . They observed high quality electrochemical performance from the batteries, which showed high areal current and power densities [54]. Pikul et al. fabricated nonporous microbatteries that showed significant increases in power density over other microbatteries and supercapacitors [53]. Others have used various etching and lithography fabrication techniques to develop 3D batteries using arrays of electrode cylinders [55] [56] [57] [58]. While placing the anode and cathode closer together decreases ion diffusion lengths in the electrolyte, such close electrode proximity can lead to a short circuit where anode and cathode come into contact. One solution is to use a solid-state electrolyte as opposed to the liquid electrolyte typically used in layer-by-layer batteries [58].

Models and simulations of some 3D battery configurations have been published. Hart et al. focused on determining an optimal electrode cylinder array configuration [59]. Zadin et al. developed an FEA electrochemical model and simulated many of the common 3D battery

architectures such as interdigitated cylinders, concentric cylinders, and interdigitated plates using a non-porous electrode (particle-scale) electrochemistry model [60]. No known studies have investigated simulating the performance of more complicated 3D battery designs, such as those simulated in this project. Evidence suggesting that 3D battery architectures based on minimal surfaces provide improved performance characteristics could influence the future direction of 3D battery design and fabrication, thus offering better performing batteries for many applications.

DETAILED DESCRIPTION OF EXPERIMENT/METHOD:

Objectives of Project

This project aims to develop capabilities to simulate lithium-ion battery electrochemistry and employ them to gain valuable insight into the effect of electrode microstructure on battery performance. The knowledge gained through this research will help explain and predict the microstructural geometrical factors that lead to improved batteries. The project has two main objectives:

- Develop a robust fully-coupled electrochemical simulation method and utilize it to simulate novel 3D battery geometries to demonstrate improvements in performance over traditional geometries and manufacturing techniques.
- Develop a three-material volume-averaged electrochemical battery model that accurately represents 3D battery microarchitectures and enables full-battery simulations in a reasonable timeframe.

This report begins with a presentation of the equations that govern the electrochemical physics relevant in a battery discharge simulation. Boundary and initial conditions as well as the finite volume discretization method that allow for numerical evaluation of the equations are discussed. Details of the solution methods and model parameters used to develop this model are also included.

The first objective of the project investigates 3D battery electrode architectures that offer potential energy density and power density improvements over traditional particle bed battery geometries. An array of electrode geometries are simulated and compared across various battery discharge rates and length scales in order to quantify performance trends and gain knowledge on geometrical factors that limit battery performance. A discussion of the studies performed and the conclusions drawn from their results demonstrates the utility of 3D electrode microstructures. An average Thiele modulus formulation is presented as a back-of-the-envelope calculation to predict the performance trends of microbattery electrode geometries. Mesh dependency results are also presented for completeness.

As a natural extension of the 3D battery particle-scale modeling, the second objective is the development and evaluation of a volume-averaged porous electrode theory formulation for these unique 3D battery geometrical conditions. It is necessary to average all three material domains (anode, cathode, and electrolyte) together, which deviates from the traditional two material volume-averaging formulation that corresponds to particle bed electrode geometries. This model is discretized and implemented in the PETSc software framework in a manner

similar to the particle-scale implementation and enables battery-level simulations of 3D battery electrode architectures. Error with respect to particle-scale results is determined to gauge the accuracy of the model and provide appropriate diffusion lengths for minimal surface electrode geometries.

Governing Equations: Particle-Scale Model

The physical processes involved in lithium-ion electrochemical battery simulations are charge and mass transport. At the electrode-electrolyte interface, Butler-Volmer kinetics are assumed to govern both charge and mass transport. In addition, charge and mass flux must be conserved across the interface. In the equations below, subscripts e and s represent the electrolyte phase and solid electrode phase (anode/cathode), respectively. The variables of interest are ϕ , representing electric potential, and c , representing lithium concentration. These equations are applied to both the anode and the cathode in a full cell sandwich simulation.

Charge is conserved within each phase, since it is assumed that no electrochemical reactions are taking place except at the electrode/electrolyte interface [28] [8] [25]. This leads to the current density conservation equation

$$\nabla \cdot (i_k) = 0 \quad (1)$$

where i represents current density and subscript k denotes phase s or e . For each phase, applying Ohm's law to Eq. (1) and including a non-dilute or concentrated solution modification for the electrolyte equation results in

$$\nabla \cdot (-\sigma_s \nabla \phi_s) = 0 \quad (2)$$

$$\nabla \cdot (-\kappa_e \nabla \phi_e) + \nabla \cdot (-\kappa_D \nabla \ln c_e) = 0 \quad (3)$$

where σ_s is electrode electrical conductivity and κ_e is electrolyte ionic conductivity [61]. The diffusional conductivity, κ_D is expressed as

$$\kappa_D = \frac{2RT\kappa_e}{F} (t_+ - 1) \left(1 + \frac{\partial \ln f}{\partial \ln c_e} \right) \quad (4)$$

where R is the universal gas constant, T is temperature, F is Faraday's constant, and t_+ is the lithium ion transference number. For this work, both temperature and lithium ion transference number are assumed to be constant. Additionally, the activity coefficient f is assumed to be constant, thus the partial derivative term in Equation (4) vanishes.

In a similar manner, the lithium species is conserved within each phase [8], yielding

$$\frac{\partial(c_s)}{\partial t} + \nabla \cdot (-D_s \nabla c_s) = 0 \quad (5)$$

$$\frac{\partial(c_e)}{\partial t} + \nabla \cdot (-D_e \nabla c_e) = 0 \quad (6)$$

It is worth noting that both Equations (3) and (6) are presented in their simplified form after applying the assumption of a constant t_+ value [24]. In reality, the transference number is concentration dependent and including that dependence could yield more physically accurate concentrated electrolyte solution behavior but resides outside the scope of this work. Additionally, mass diffusivities (D_s , D_e) and conductivities (σ_s , κ_e) are assumed to be constant values.

A widely accepted approach used to model the electrochemical charge transport across electrode/electrolyte interfaces is the use of Butler-Volmer kinetics relations [61]. The Butler-Volmer kinetic equation governs the interface current density, j , as

$$j = i_0 \left[\exp\left(\frac{\alpha_a F}{RT} \eta\right) - \exp\left(-\frac{\alpha_c F}{RT} \eta\right) \right] \quad (7)$$

where i_0 is the exchange current density and α_a and α_c are anode and cathode constants, taken to be 0.5. The exchange current density is represented by

$$i_0 = kF(c_e)^{\alpha_a}(c_{s,max} - c_s)^{\alpha_a}(c_s)^{\alpha_c} \quad (8)$$

where k is the Butler-Volmer reaction rate constant and $c_{s,max}$ is the maximum intercalated lithium concentration allowed for the given electrode material [24]. The local overpotential at the interface, η , is defined as

$$\eta = \phi_s - \phi_e - U \quad (9)$$

where U is a function representing the open-circuit potential (OCP) corresponding to the local state of charge, θ , defined as

$$\theta = \frac{c_s}{c_{s,max}} \quad (10)$$

The experimental OCP dependence on θ can be fit to a polynomial function and is used analytically for battery modeling [61]. All lithium concentration (c_s , c_e) and potential (ϕ_s , ϕ_e) variables used in the Butler-Volmer equation are located on the electrode/electrolyte interface.

Governing Equations: Volume-Averaged Model

As mentioned in the introduction, traditional battery simulation efforts use a volume-averaged model to represent the electrochemistry and transport physics during a battery discharge. Such reduced-order models are necessary as a particle-scale simulation on an entire battery cell is computationally infeasible. The ability to accurately simulate a full battery is a necessary step in the scale up of the 3D microbattery architectures. Therefore, as a natural extension of the particle-scale work, the resolved particle-scale equations presented in the previous subsection are volume-averaged assuming that both anode and cathode are present throughout the battery volume, resulting in a three-material volume-averaged battery model suitable for simulating 3D battery architectures.

The volume-averaged equations presented here follow a similar process to the original porous electrode theory developed by Newman and Tiedemann [26] and the volume-averaging process is detailed elsewhere [62]. This modeling effort is macroscopic in nature and disregards the detailed geometrical microstructure of the electrodes and electrolyte. All solution variables are assumed to be continuous and exist at every point in the battery domain. Here we assume that the battery consists of three superimposed continuous regions: anode, cathode, and electrolyte. A representative elemental volume (REV) is used to average the equations and solution variables [27] [61]. The conservation statements presented in the particle-scale model equations are still valid and volume-averaging Eqs. (2)-(7) over an REV results in the set of scalar transport equations

$$\nabla \cdot (-\sigma_{s,a}^{eff} \nabla \langle \phi_{s,a} \rangle) + a_a \bar{J}_a = 0 \quad (11)$$

$$\nabla \cdot (-\sigma_{s,c}^{eff} \nabla \langle \phi_{s,c} \rangle) + a_c \bar{J}_c = 0 \quad (12)$$

$$\nabla \cdot (-\kappa_e^{eff} \nabla \langle \phi_e \rangle) + \nabla \cdot (-\kappa_D^{eff} \nabla \ln \langle c_e \rangle) - a_a \bar{J}_a - a_c \bar{J}_c = 0 \quad (13)$$

for charge conservation, and similarly

$$\frac{\partial(\epsilon_{s,a} \langle c_{s,a} \rangle)}{\partial t} + \nabla \cdot (-D_{s,a}^{eff} \nabla \langle c_{s,a} \rangle) + \frac{a_a \bar{J}_a}{F} = 0 \quad (14)$$

$$\frac{\partial(\epsilon_{s,c} \langle c_{s,c} \rangle)}{\partial t} + \nabla \cdot (-D_{s,c}^{eff} \nabla \langle c_{s,c} \rangle) + \frac{a_c \bar{J}_c}{F} = 0 \quad (15)$$

$$\frac{\partial(\epsilon_e \langle c_e \rangle)}{\partial t} + \nabla \cdot (-D_e^{eff} \nabla \langle c_e \rangle) - (1 - t_+) \frac{a_a \bar{J}_a}{F} - (1 - t_+) \frac{a_c \bar{J}_c}{F} = 0 \quad (16)$$

for species conservation. Subscripts s, a ; s, c ; e correspond to values in the solid anode, solid cathode, and electrolyte phases, respectively. Throughout this section brackets are used to indicate a volume-averaged value. As in the previous sections, $\langle c \rangle$ represents volume-averaged lithium concentration, and $\langle \phi \rangle$ represents volume-averaged electric potential. t_+ is the lithium ion transference number and is assumed to be constant. It is worth noting that both Equations

(13) and (16) are presented in their simplified form after applying the assumption of a constant t_+ value [27]. From the volume-averaging process, material volume fraction (ϵ) is introduced into the unsteady terms of the species equations.

Each scalar transport equation (11)-(16) contains a diffusion coefficient that is assumed to remain constant. It is important to note that diffusion coefficients in these volume-averaged equations are effective properties and are not intrinsic material properties. Effective properties are usually estimated using an analytical relationship. The common relationship used to obtain effective properties in porous electrode theory battery simulations is Bruggeman's approximation [63]. This applies to mass diffusivity (D), electric conductivity (σ), and ionic conductivity (κ), which can be related to corresponding intrinsic properties by

$$D^{eff} = D(\epsilon)^{1.5} \quad (17)$$

$$\sigma^{eff} = \sigma(\epsilon)^{1.5} \quad (18)$$

$$\kappa^{eff} = \kappa(\epsilon)^{1.5} \quad (19)$$

where ϵ represents material volume fraction.

One of the major differences between the particle-scale model and the volume-averaged model is the treatment of the reaction rate term. Recall that the reaction between electrode and electrolyte is governed by Butler-Volmer interface kinetics, where the interface current density is defined by Equations (7)-(10). Divergence theorem is used to volume-average the Butler-Volmer current density, j_k

$$\iint \nabla \cdot j_k dA_k = a_k \bar{j}_k \quad (20)$$

where a_k is the specific surface area defined as the ratio of reactive surface area for electrode k in the REV to the total REV volume. For a particle bed, the specific surface area can be analytically related to particle radius and volume fraction by assuming that the porous electrode is composed of small spheres of a single size. Alternatively, surface areas and volumes can be obtained directly from the 3D battery microarchitecture, which is the approach used throughout this section. While j is defined by equations (7)-(10), it assumes species concentration and potential variables are electrode/electrolyte interface values. We define here that for each REV

$$\bar{j}_k = j(\bar{\phi}_{s,k}, \bar{\phi}_e, \bar{c}_{s,k}, \bar{c}_e) \quad (21)$$

where a barred variable ($\bar{}$) denotes interface values averaged over the entire electrode/electrolyte interface within the REV and k again represents a generic electrode type of either anode (a) or cathode (c) in the transport equations. The relationship between averaged interface surface values required by this equation and volume-averaged values is discussed next.

As mentioned and observed elsewhere in this report, solid phase diffusion in the electrode is typically rate limiting and must be represented in the volume-averaged model [22]. We assume that the other variables of interest (concentration in the electrolyte and electric potential

values) are relatively uniform within an REV, thus we can define most of the variables required by Eq. (21) as

$$\bar{\phi}_{s,k} = \langle \phi_{s,k} \rangle \quad (22)$$

$$\bar{\phi}_e = \langle \phi_e \rangle \quad (23)$$

$$\bar{c}_e = \langle c_e \rangle \quad (24)$$

Capturing solid phase diffusion is a point of emphasis within previous volume-averaged battery modeling work. Since we plan to simulate batteries with unique electrode microstructural shapes such as those based off of minimal surfaces presented in this report, a method that does not require simplistic electrode shapes is desired. The diffusion length method developed by Wang et al. [28] [29] allows for generic treatment of solid phase diffusion by assuming a linear relationship between the solid surface concentration and the volume-averaged concentration within the solid. Using their method and bearing in mind that our governing equations have been formulated with the convention that \bar{j}_k is the average interface current leaving the electrode (see Eqs. (33)-(36)) in direction \mathbf{n} , introducing the diffusion length (l_d) yields the interface relationship

$$\frac{\bar{j}_k}{F} = -D_{s,k} \frac{\partial c_s}{\partial \mathbf{n}} = -D_{s,k} \frac{\bar{c}_{s,k} - \langle c_{s,k} \rangle}{l_{d,k}} \quad (25)$$

for each electrode k [28]. As diffusion through a length of the solid material is being modeled, the mass diffusivity ($D_{s,k}$) used here is the intrinsic property value. Solving for $\bar{c}_{s,k}$ yields a more useful form:

$$\bar{c}_{s,k} = \langle c_{s,k} \rangle - \frac{\bar{j}_k l_{d,k}}{F D_{s,k}} \quad (26)$$

Wang et al. analytically derived l_d values for simple shapes. They state that one should use l_d values of $R/5$ for spherical shapes, $R/4$ for cylindrical shapes, and $L/3$ for plate-like shapes, where R is sphere/cylinder radius and L is plate half-thickness [28].

It was demonstrated that assuming the previous linear relationship and therefore assuming a steady-state profile introduces significant inaccuracy during the early portion of a discharge when the concentration profile has not yet developed. Comparing to the exact solution obtained from Duhamel's superposition for several simple geometries (sphere, cylinder, plate), a time-dependent (t) correction of the form

$$\bar{c}_{s,k} = \langle c_{s,k} \rangle - \frac{\bar{j}_k l_{d,k}}{F D_{s,k}} \left(1 - e^{-\frac{4\sqrt{D_{s,k}}t}{3l_{d,k}}} \right) \quad (27)$$

was introduced. This correction factor was shown to yield consistent error-reducing results for several electrode geometries [29]. Equations (22), (23), (24), and (27) bring closure to Equation (21) and complete the model.

Boundary Conditions

The boundary conditions for the scalar transport Eqs. (2), (3), (5) and (6) are shown on a simplified 2D battery cell image in Figure 1. In the figure, lines AB and CD represent current collector interfaces, where current enters and leaves the domain. No lithium is allowed to leave the battery, so the species transport boundary conditions at the current collector boundaries can be described as the Neumann boundary conditions

$$\mathbf{n} \cdot \nabla c_s = 0 \text{ at } x = 0, W \quad (28)$$

and

$$\mathbf{n} \cdot \nabla c_e = 0 \text{ at } x = 0, W \quad (29)$$

where \mathbf{n} denotes the outward normal vector on each respective boundary, except where otherwise noted. Here, x represents the coordinate direction along the battery width, and W is the battery width, or distance between boundaries AB and CD. In practical use, current is supplied through metallic current collectors on either end of the battery (typically copper and aluminum). In the present model, current collectors are not included in the computational domain. Instead, boundary conditions are applied directly to the electrodes where the current collectors would connect. The current condition applied at the CD boundary to the cathode material is

$$\mathbf{n} \cdot (-\sigma_s \nabla \phi_{s, cathode}) = I_{app} \text{ at } x = W \quad (30)$$

where I_{app} is the specified applied current density leaving the cathode boundary during the battery discharge. In order to set the level of cell voltage and yield a unique solution, a Dirichlet boundary condition of an arbitrary value of 0 volts is set for the anode material at the AB boundary, yielding

$$\phi_{s, anode} = 0 \text{ at } x = 0 \quad (31)$$

Electrical current can only flow out of the computational domain through the current collectors, *i.e.*, only through the electrode material current collector boundary. This yields a zero current condition of

$$\mathbf{n} \cdot (\kappa_e \nabla \phi_e + \kappa_D \nabla \ln c_e) = 0 \text{ at } x = 0, W \quad (32)$$

on the electrolyte region of the current collector boundaries AB and CD.

Lines AC and BD represent cuts through the battery cell where the material geometries continue for a distance much longer than the battery width. These cuts are necessitated by computational feasibility as the entire microstructure, millimeters to centimeters in size, would

be prohibitively expensive to simulate. Although the image is 2D, similar cuts are made in the third dimension as well (into and out of the page) for 3D simulations. Since all of the electrode geometries discussed in this work are inherently periodic, these boundaries are modeled as periodic boundaries, where the model assumes that opposite boundaries are adjacent to one another [24]. Boundary and initial conditions for the volume-averaged equations are similar to those applied to the particle-scale model.

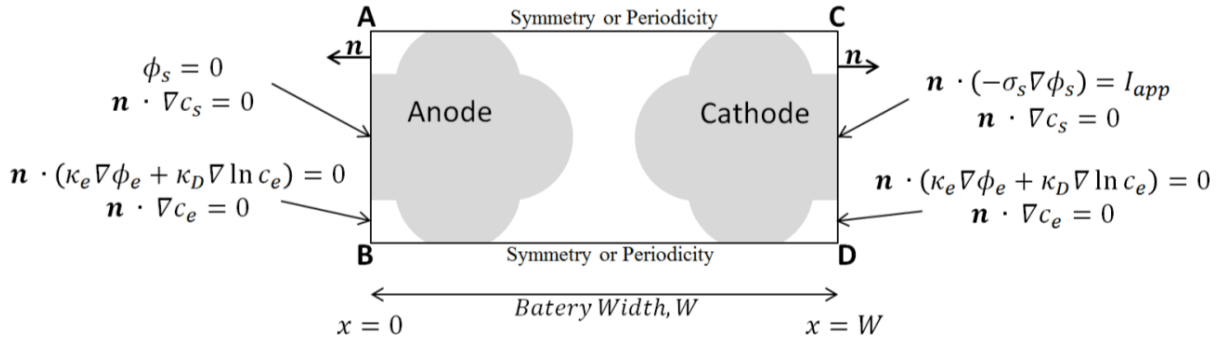


Figure 1. Boundary conditions for battery discharge simulation

Interface Conditions

As previously mentioned, Butler-Volmer kinetics govern the interface current density as a function of local species concentrations as well as local electric potentials. Neither potential nor species concentration are continuous across an interface ($c_s \neq c_e$, $\phi_s \neq \phi_e$). Thus, a total of four interface equations governing interface transport behavior are required. The two equations corresponding to the species transport are

$$\mathbf{n} \cdot (-D_e \nabla c_e) = (1 - t_+) \frac{j}{F} \quad (33)$$

$$\mathbf{n} \cdot (-D_s \nabla c_s) = \frac{j}{F} \quad (34)$$

where \mathbf{n} is the interface normal vector pointing from the electrode into the electrolyte. Similarly, the two additional interface equations for the potential equations are

$$\mathbf{n} \cdot (-\kappa_e \nabla \phi_e + \kappa_D \nabla \ln c_e) = j \quad (35)$$

$$\mathbf{n} \cdot (-\sigma_s \nabla \phi_s) = j \quad (36)$$

Equations (33) through (36) represent interface mass transport and current, governed by the Butler-Volmer relationship. Since all transport at a given point on the interface is governed by the same j value, these interface equations enforce balance of species flux and balance of electric

current [28]. This model neglects any solid-electrolyte interface (SEI) layer formation, so the interface between electrode and electrolyte cannot store species nor charge, and thus, flux balance is required. Equation (33) accounts for the fact that in the electrolyte not all charge is carried by lithium ions, an effect quantified by the lithium transference number (t_+).

Numerical Methods – Finite Volume Method

The governing equations are discretized using the finite-volume method (FVM) discretization scheme, which has been detailed elsewhere [64] and is briefly described here for completeness [65]. This discretization applies to both the particle-scale model and the volume-averaged model. The computational domain is divided into arbitrary convex polyhedral cells. The variable of interest, either species concentration or potential, is stored at the cell centroids. The governing transport equations for species transport and electric potential, Eqs. (2)-(6), are integrated over the cell volumes to provide cell balances of species and potential flux, unsteady terms, source terms, and boundary conditions [66].

All four partial differential equations can be described by the generic scalar transport equation

$$\frac{\partial}{\partial t}(\varphi) + \nabla \cdot \mathbf{J} = S \quad (37)$$

where φ is the variable of interest, \mathbf{J} is the variable flux, and S is the source term. After applying a control volume balance and the divergence theorem, Eq. (37) results in

$$\int_{\Delta V} (\varphi^1 - \varphi^0) dV + \int_{\Delta t} \int_A \mathbf{J} \cdot d\mathbf{A} dt = \int_{\Delta t} \int_{\Delta V} S dV dt \quad (38)$$

where V is cell volume, A is cell surface area, and superscripts 1 and 0 denote values of φ at times $t + \Delta t$ and t , respectively. A second order spatial scheme as well as an implicit temporal scheme are applied to discretize the unsteady and diffusion flux terms in Eq. (38) [66].

Linearization of Interface Conditions

Determining Jacobian matrix values for the diffusive terms in the governing equations is straightforward since the finite volume discretization assumes a linear relationship between neighboring cells. In contrast, numerically implementing equations (33) through (36) involve some complexity, as they are nonlinear in all four variables of interest at the interface and thus require a nonlinear solution procedure such as Newton's method. In order to determine the Jacobian matrix values for the linear system, a linearization of the Butler-Volmer current density is performed using a truncated Taylor series expansion:

$$j = j^* + \left(\frac{\partial j}{\partial c_s}\right)^* (c_s - c_s^*) + \left(\frac{\partial j}{\partial c_e}\right)^* (c_e - c_e^*) + \left(\frac{\partial j}{\partial \phi_s}\right)^* (\phi_s - \phi_s^*) + \left(\frac{\partial j}{\partial \phi_e}\right)^* (\phi_e - \phi_e^*) \quad (39)$$

where the star superscript (*) denotes a term evaluated at prevailing values. At convergence, these variables will equal their starred values and thus Eq. (39) yields a solution that is independent of the approximations made in the linearization. The necessary partial derivative terms are calculated analytically from Eq. (7).

Furthermore, the finite volume methodology stores solution variables at the cell centroid, and Eq. (39) requires interface values. Using the definition for interface flux given by Eqs. (33)-(36) and assuming a typical finite volume method linear solution profile between storage sites on a hexahedral grid, the interface values required by Eq. (39) can be represented in terms of the cell centroid values by

$$-FD_s \frac{c_{s,int} - c_{s,centroid}}{\Delta x/2} = j^* \quad (40)$$

and

$$FD_e \frac{c_{e,int} - c_{e,centroid}}{\Delta x/2} = (1 - t_+) j^* \quad (41)$$

for the lithium interface surface concentration values and in a similar manner for the potential interface surface values. Here \mathbf{x} represents a Cartesian coordinate $x, y, \text{ or } z$.

Thiele Modulus

Using a dimensionless metric to evaluate the reaction vs. diffusion characteristics of each battery geometry at various discharge currents may provide additional insight and predict performance trends without requiring a full electrochemical discharge simulation. This dimensionless quantity, the Thiele modulus (h_T), is defined as

$$h_T = \frac{\text{diffusion time}}{\text{reaction time}}, \quad h_T^2 = \frac{k_n L_c^2}{D_s} \quad (42)$$

where k_n is a first-order reaction rate term in s^{-1} , L_c is the characteristic diffusion length, and D_s is the ionic or mass diffusivity [67] [68]. This metric provides some insight into when a discharge will be reaction or diffusion limited as well as offers a rough evaluation of an electrode geometry's ability to perform well. To estimate the first-order reaction rate k_n for each simulation, the following equations are used.

$$k_n'' = \frac{j''}{C_{Li}F} \quad (43)$$

$$k_n = k_n'' \frac{A_{BV}}{V} = \frac{j'' A_{BV}}{C_{Li} F V} = \frac{I_{app} A_{CC}}{C_{Li} F V} \quad (44)$$

Here k_n'' is the reaction rate per unit surface area, A_{BV} is the reaction surface area, V is the active material volume, j'' is the Butler-Volmer current density in A/m^2 , C_{Li} is the surface concentration of lithium in mol/m^3 , and F is Faraday's constant. From conservation, we know the total Butler-Volmer current, $j'' \cdot A_{BV}$, must equal the applied boundary current, $I_{app} \cdot A_{CC}$, where A_{CC} is the current collector boundary area. C_{Li} varies throughout the battery discharge and therefore must be approximated here. In the electrolyte, gradients are small compared to those in the electrode, so an L_c value equivalent to the electrolyte feature size and a C_{Li} value equivalent to the average electrolyte concentration are used. We expect large concentration gradients in the electrode, so we should not assume that the surface lithium concentration C_{Li} is equivalent to the overall lithium concentration C . We use a simple linear diffusion approximation, where the concentration profile in the electrode is assumed to be parabolic, similar to the diffusion length method developed by Wang et al. [28]:

$$j'' A_{BV} = I_{app} A_{CC} = F D_s A_{BV} \frac{C - C_{Li}}{L_c} \quad (45)$$

where C is set to the initial lithium concentration of the material. L_c is equivalent to $L/3$ for a plate geometry where L is the plate half-thickness. Similarly, L_c is equivalent to $R/4$ for a cylindrical geometry and $R/5$ for spherical particles where R is the cylinder/sphere radius [28]. If such an approximation yields an unphysical negative value for surface concentration, it is assumed to be very low (1 mol/m^3). Combining Eqns. (44) and (45) yields our approximated k_n value.

$$k_n = \frac{I_{app} A_{CC}}{(C - \frac{I_{app} A_{CC} L_c}{F D_s A_{BV}}) F V} \quad (46)$$

Using these definitions, the estimated Thiele modulus can be calculated a priori based on geometric parameters for each discharge rate.

PETSc Implementation: Particle-Scale Model

The particle-scale model and corresponding numerical discretization described in the previous sections have been implemented within the PETSc software framework [69] [70], chosen for its distributed-memory data structures, scalable implementations of a wide variety of numerical methods, and portability.

All battery geometries subsequently discussed are created within the PETSc code and have been included as run-time options along with other parameters such as mesh and domain size in all three dimensions, discharge current, time step size, etc. The PETSc implementation only allows for simulation on hexahedral structured meshes, since implementing an unstructured discretization scheme would have been a significant technical challenge. While hexahedral non-conformal meshes cannot capture the true geometrical shape or surface area of a structure, they provide an approximate geometry and allow trends to be discerned across similar simulations. For the simulations presented, a finite volume cell size of approximately $0.667 \times 0.667 \times 0.667$

μm^3 was used, allowing for consistent comparison across simulations. A mesh size dependence study is presented later, validating this mesh size choice. Even though cubic cells were typically used, the implementation allows for different discretization sizes in all three dimensions.

The discretized conservation equations (Eqs. (2), (3), (5) and (6)) and associated interfacial (Eqs. (33)-(36)) and boundary conditions (Eqs. (28)-(32)) form a collection of ODEs that fully couple the concentration of lithium ions and electrical potential in both phases. These ODEs were solved using the theta method. [70]. A theta value of 0.5 is used (equivalent to a 2nd-order implicit midpoint method), except for the first several time steps where $\theta = 1.0$ (equivalent to a backward Euler method). This procedure is analogous to variable-order ODE solvers, which use lower-order methods to bootstrap higher-order methods. Nonlinear equations were solved using a Newton method with line search; within the Newton method, linear systems were solved using a stabilized biconjugate gradient method, left-preconditioned by the BoomerAMG implementation of algebraic multigrid from the hypre package [71]. For completeness, the command-line options used included: theta time step extrapolation, absolute residual tolerances of $1\text{e-}17$ for both linear and nonlinear solvers, and a relative linear solver tolerance of $1\text{e-}2$.

The battery is considered discharged when the potential difference across the current collector boundaries reaches a value less than 2.95 Volts. Each battery discharge simulation is discretized into approximately 500-1000 time steps (based on theoretical energy density), solved over $\sim 800,000$ finite volume cells, and computation/storage is split across 36-48 cores on Intel Xeon 5680 processors [72]. Each simulation presented took 2-18 hours to complete, depending on geometry, discharge current, and time step size.

PETSc Implementation: Volume-Averaged Model

The finite volume method is applied to scalar transport governing Equations (11)-(16) to yield a discretized set of equations. While the equation set is effectively 1D due to the use of periodic boundary conditions, the equations are numerically implemented in all three dimensions to keep the model generic. This allows for further considerations such as anisotropic diffusion or full-cell simulations with unique boundary conditions to be implemented with little effort. The volume-averaged model contains six scalar transport equations or field variables ($c_{s,a}, c_{s,c}, c_e, \phi_{s,a}, \phi_{s,c}, \phi_e$), while the particle-scale model only consists of two (c and ϕ). However, since the microstructure does not need to be resolved, the volume-averaged model operates on much coarser meshes resulting in significantly fewer degrees of freedom in the physical domain.

Using many of the same PETSc data structures and methods described in the previous subsection, the volume-averaged model can be solved in a fully-coupled stable algorithm on a hexahedral mesh [70]. There is strong inter-equation coupling here as each equation contains a \bar{j}_k term. The ODEs are solved using the theta method. A fully analytic Jacobian matrix is computed, and a Newton method with line search is used with a stabilized biconjugate gradient iterative linear solver. The boomerang algebraic multigrid preconditioner (from Hypre [71]) is also used to accelerate the convergence of the linear solver. By nature of volume-averaging, the only microstructural information required by the model are volume fractions ($\epsilon_e, \epsilon_{s,a}, \epsilon_{s,c}$), electrode surface area to volume ratios, and electrode diffusion lengths ($l_{d,a}, l_{d,c}$). Run-time

options include mesh and domain size in all three dimensions, discharge current, and time step size.

Due to the highly non-linear nature of the Butler-Volmer current equation, the prevailing \bar{j}_k value used in Equation (27) was underrelaxed. Underrelaxation coefficient (α) values ranging from 0.15-0.3 provided the most stable convergence depending on discharge current [64]. Even though the source terms in Eqs. (11)-(16) contain \bar{j}_k , underrelaxation there was not necessary. We also found that a gradual ramp-up of the l_d value during the first time step allowed for stable behavior for all simulations performed for this project.

Electrode geometries and properties

In general, the computational domain for a battery simulation consists of two electrode regions and an electrolyte region. In reality, the space between the electrodes is filled with a porous separator, electrolyte, and binder, but for most simulations including those performed here, the separator region is assumed to be filled with electrolyte alone. Figure 2 shows a typical synthetically generated computational domain that was created using the CUBIT software [73].

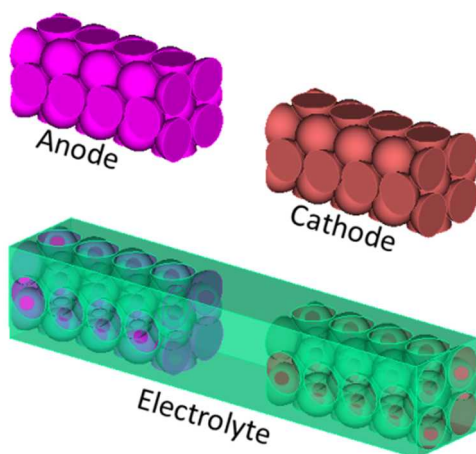


Figure 2. Representation of synthetic computational domain

All simulations used material property parameters in Table 1 and model parameters in Table 2. These properties were obtained from the often-cited volume-averaged pseudo-2D full cell simulation studies by Doyle and Newman, where a graphite anode and a LiMn_2O_4 cathode are used [27]. Other electrode materials may be simulated by modifying material property parameters accordingly; for the purpose of comparing electrode geometries, these materials were chosen.

Table 1. Material property parameters used in simulations

Material Property	Li _y Mn ₂ O ₄ Cathode	Electrolyte	Li _x C ₆ Anode
Li/Li ⁺ Mass Diffusivity, D (m ² /s)	1.00E-13	7.50E-11	3.90E-14
Solid Phase Conductivity, σ_s (S/m)	3.8		100
Electrolyte Ionic Conductivity, κ_e (S/m)		0.2	
Initial Li Concentration, c^0 (mol/m ³)	3900	2000	14780
Maximum Concentration, $c_{s,max}$ (mol/m ³)	22860		26390

Table 2. Model parameters used in simulations

Model Parameter	Value
Temp (K)	300
Li Transport Number, t_+	0.363
α_a, α_c	0.5
Butler-Volmer Constant, k (m ^{2.5} mol ^{-0.5} s ⁻¹)	1.10E-11

1D and 2D Battery Electrode Geometries

As previously discussed, batteries are traditionally manufactured using a cell sandwich approach, where the anode region and cathode region are completely separated. The simplest form of battery architecture is effectively 1D and consists of thin slabs of anode, separator/electrolyte, and cathode between current collectors as shown in Figure 3. This figure and subsequent depictions of computational geometries follow the convention that red denotes anode active material, black denotes cathode active material, and grey denotes electrolyte material. Since ions need to flow from anode to cathode through an interface reaction, a larger active material surface area to volume ratio decreases the surface reaction current density (j) for a given applied boundary current. Equations (33)-(36) stipulate that a decreased reaction density reduces results in smaller concentration gradients being formed and is therefore desirable. This high surface area requirement leads to the particle bed architecture exhibited by modern lithium-ion batteries as represented in Figure 2 and Figure 4. The porous anode and cathode regions are composed of a connected network of active material particles, with liquid electrolyte filling the void space. These architectures will be simulated to serve as a comparison for the 3D battery architectures. The particles geometry considered here is a synthetic geometry that is composed of spherical particles packed in a body centered cubic type orientation and of radius 8 μm due to material choices discussed previously [27]. While the particle centroids are spaced assuming an 8 μm radius, a radius of 8.15 μm is used when creating the geometry to ensure particle overlap and therefore form a continuous particle network. This geometry can be described as 2D due to the approximately symmetric diffusion of lithium ions to the surface of the electrode particles, thus reducing the dimension. The overall physical dimensions of the synthetic particle bed are 203 \times 38 \times 38 μm^3 , with anode and cathode region thicknesses of 92 μm each and a separator region thickness of 18 μm . Additionally, active material volume fractions for both the anode and cathode are approximately 0.71, which has been recently shown to be experimentally accurate [34]. For both geometries shown here, the anode current collector boundary condition is applied to the left surface and cathode current collector condition to the right surface.

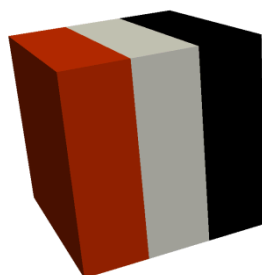


Figure 3. Films (1D)

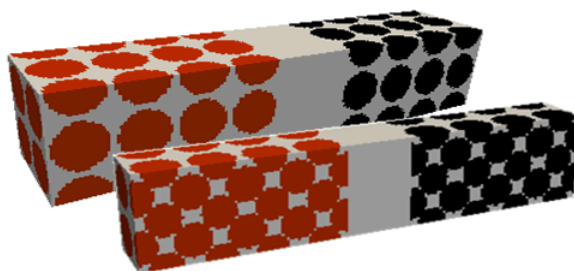


Figure 4. Particle bed cell sandwich geometry

3D Battery Electrode Geometries

As mentioned during in the introduction, interpenetrating electrode configurations, or 3D batteries, have been proposed as a method to improve battery performance by shortening ion path lengths. Various 3D battery geometries are considered here. Appropriate additive manufacturing techniques for each microstructure are not discussed here as the focus is to determine the performance characteristics of such geometries assuming manufacturability. Several 2D extrusions that yield 3D batteries are included as simple geometries that lend themselves to additive manufacturing. While we refer to these battery architectures as 3D batteries due to the interpenetrating nature of the anode and cathode, they can also be considered psudeo-2D since diffusion through the electrode can be assumed to be axially symmetric. The first is an alternating plate geometry, shown in Figure 5, where anode and cathode plates alternate with electrolyte filling the gaps between. The second extruded geometry considered is an array of cylinders, shown in Figure 6. This 2D geometry is extruded into and out of the page to yield a 3D battery architecture of the desired width. The anode and cathode current collectors are placed parallel with the page plane on opposite ends of the extruded geometry. While other configurations of cylinders are possible, this was chosen due to its repeatability and equal volume fractions of anode and cathode active material.

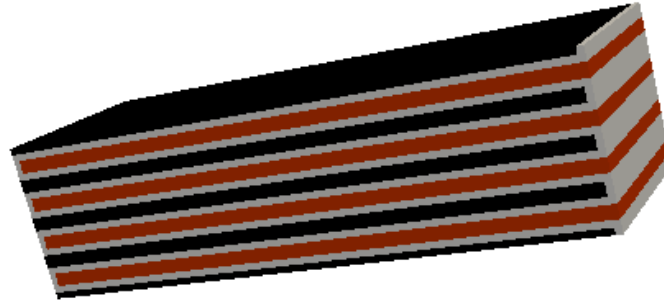


Figure 5. Extruded plates

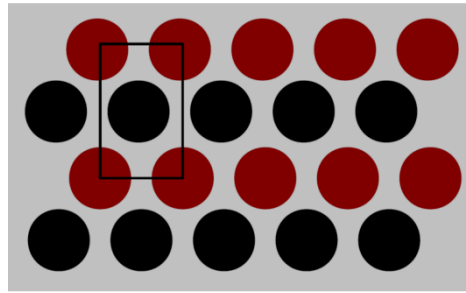


Figure 6. Extruded cylinder array with unit cell outlined

Two truly 3D electrode geometries, where an axis of symmetry is not apparent, are also introduced. These electrode structures are based on a group of mathematical surfaces defined as minimal surfaces. The two topologies used for this study are the Schwarz P and the gyroid [74] [75]. They are triply periodic and define a bi-continuous pore space, thus allowing for an interpenetrating anode/cathode geometry. For these surface structures, a unit cell is defined as one repeating geometric unit.

A unit cell of the Schwarz P surface topology is shown in Figure 7 and the surface is approximated by $F_{\text{Schwarz P}}(x, y, z) = 0$, where the Schwarz P function is defined as

$$F_{\text{Schwarz P}}(x, y, z) = \cos\left(\frac{2\pi}{L}x\right) + \cos\left(\frac{2\pi}{L}y\right) + \cos\left(\frac{2\pi}{L}z\right) \quad (47)$$

where x , y , and z are Cartesian coordinates in the physical domain and L is the cubic unit cell edge length. The gyroid surface topology unit cell is shown in Figure 8 and is approximated by $F_{\text{gyroid}}(x, y, z) = 0$ where the gyroid function is

$$F_{\text{gyroid}}(x, y, z) = \sin\left(\frac{2\pi}{L}y\right)\cos\left(\frac{2\pi}{L}z\right) + \sin\left(\frac{2\pi}{L}z\right)\cos\left(\frac{2\pi}{L}x\right) + \sin\left(\frac{2\pi}{L}x\right)\cos\left(\frac{2\pi}{L}y\right) \quad (48)$$

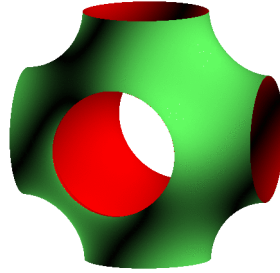


Figure 7. Schwarz P minimal surface

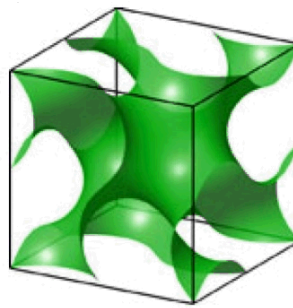


Figure 8. Gyroid minimal surface

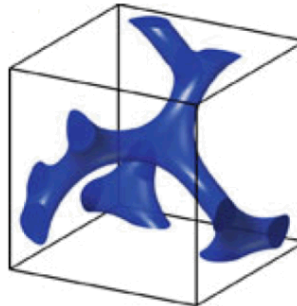


Figure 9. $F_{gyroid}(x,y,z) > t$, $t = 1.3$

Setting Eq. (47) and Eq. (48) equal to a value other than zero represents a surface resembling a hollow shell [76] [77]. If one considers any evaluation of $F_{gyroid}(x,y,z)$ greater than t as a solid structure, effectively filling in the shell, the unit cell geometry shown in Figure 9 results. Using these functions to create anode/electrolyte/cathode interpenetrating structures requires a double Schwarz P and a double gyroid. A double gyroid geometry is obtained when one material is defined by $F_{gyroid}(x,y,z) > t$ and a second material is defined by $F_{gyroid}(x,y,z) < -t$ [77]. The t values of the double gyroid can vary independently to obtain interpenetrating structures of desired thicknesses. This same process can be applied to the Schwarz P function to obtain two distinct interpenetrating triply periodic structures. Example computational electrode representations of these geometries are shown in Figure 10 and Figure 11. Values of t have been

chosen here such that anode and cathode active material volume fractions are approximately equal.



Figure 10. Double gyroid structure with $t = 0.6$

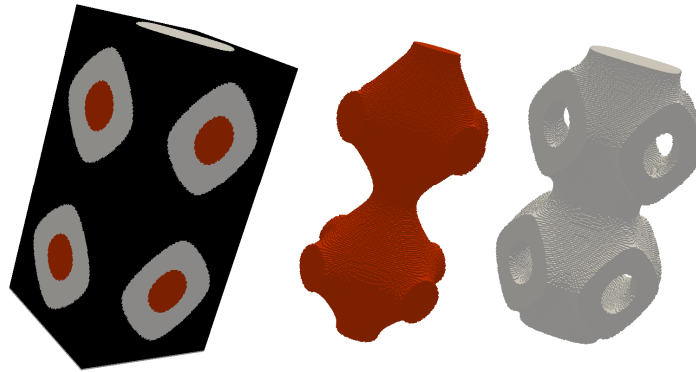


Figure 11. Double Schwarz P structure with $t = 0.56$

Quantities of Interest

Two important parameters that characterize battery performance are power density and energy density. These values can be scaled as volumetric, areal, or gravimetric densities. Energy density is proportional to the total energy supplied by the battery throughout a discharge cycle and power density is proportional to the rate at which that energy is provided. As discussed in the introduction, in addition to cycle life and stability, power and energy densities are a focal area for battery improvement. A tradeoff between power density and energy density exists and is best exhibited by a Ragone plot, which plots the two quantities against each other [78]. For this project, Ragone plots will be used to demonstrate the performance comparison between the previously described electrode geometries. Power density is obtained from a full battery discharge by $Power\ Density = \frac{V \times I_{app}}{Vol}$ where V is time-averaged cell voltage averaged over the entire discharge time, I_{app} is the applied current, and Vol is the total battery volume. We define cell voltage as the difference between the potential (ϕ_s) at the cathode current collector boundary and that at the anode current collector boundary, where potential values at those locations are

spatially averaged across the entire boundary area. Energy density is then evaluated by $\text{Energy Density} = \text{Power Density} \times \text{Discharge Time}$.

Two geometric parameters are of interest. The first is surface area to volume ratio (SA/V ratio). The definition used throughout this work is $\text{SA/V Ratio} = \frac{\text{Interface area between electrode and electrolyte}}{\text{Volume of electrode active material}}$. This is an important ratio that is similar to a model parameter (specific surface area, a) that appears in the volume-averaged electrochemical equations, presented earlier. A higher SA/V ratio results in more surface area for the interface Butler-Volmer reaction to take place, thus allowing faster overall interface transport. The second geometrical parameter used to describe these geometries is *minimum feature size*. When discussed here, feature size refers to the thickness of a particular portion of a structure. The minimum feature size becomes an important geometrical characteristic when considering the manufacturability of a 3D geometry. Any additive manufacturing technique has a lower limit on feature resolution, thus requiring a manufacturable geometry to have a minimum feature size equal to or greater than that resolution.

RESULTS:

Several studies are performed to demonstrate and evaluate the performance characteristics. These studies start with comparisons between 3D battery and particle bed battery simulations. After establishing the 3D battery performance improvements suggested by our simulations, the various electrode microstructures are compared to each other. These comparisons will serve to guide 3D battery experiments and manufacturing by demonstrating theoretical performance characteristics for the various microstructures. Comparisons are presented for three sets of microstructural requirements: electrode surface area to volume ratio (SA/V), minimum electrolyte feature size, and minimum electrode feature size.

Uniform Surface Area to Volume Ratio Comparison

In order to evaluate the geometrical effects of the various proposed electrode microstructures, a comparison between geometries with more parameters held to uniform values is required. For this study, the particle bed geometry shown in Figure 4 was constructed in accordance with the battery and particle sizing discussed previously. Subsequently, the other geometries were constructed to match several attributes. First, the cell width or distance between current collector boundaries was held constant at 203 μm , except for the films geometry where the battery width is set by the three film thicknesses. In addition, geometric parameters such as gyroid/Schwarz P thickness, plate thickness, cylinder radius, etc. were adjusted to values that resulted in material volume fractions that approximately matched those displayed in the particle bed geometry. This ensured that all batteries compared have similar theoretical energy densities and any performance differences were not due to varying amounts of active material. Lastly, the relative size (unit cell size) of each geometry was set so that the SA/V ratio would be approximately uniform across all geometries. This gave each geometry an equal amount of surface area for the interfacial reaction to occur, which plays a major role in determining the formation of concentration gradients as previously mentioned. Holding these parameters

constant across all simulations isolates performance differences due to geometric effects. Such a study will allow us to understand if any transport limitations arise due to geometry.

Table 3 provides the necessary unit cell sizes and resulting meshed SA/V ratio as well as minimum electrode and electrolyte feature sizes for the constant SA/V ratio comparison. Simulations were performed on all geometries at discharge currents of 5, 10, 20, 40, 80, 160, and 320 A/m², where a current of 20 A/m² corresponds to a discharge rate of approximately 1C. Figure 12 contains a Ragone plot of the resulting sweep of discharge simulations.

Table 3. Geometry characteristics for uniform SA/V comparison

Geometry	Electrode Feature (μm)	Electrolyte Feature (μm)	SA/V x 10 ⁻⁸ (1 / m)	Unit Cell Size (μm)	Size Parameter
Gyroid	10.5	4.4	4.53	31 x 31 x 31	L = 31 μm t _{anode} = t _{cathode} = 0.54
Schwarz P	7.5	4.5	4.60	24 x 24 x 24	L = 24 μm t _{anode} = t _{cathode} = 0.61
Plate	4.4	2.3	4.59	13.4	
Cylinder	11	2.05	4.55	13 x 22.5	Radius = 5.5 μm
Film	2.2	2.2	4.55	6.6	
Particles	-	-	4.55	-	Radius = 8 μm

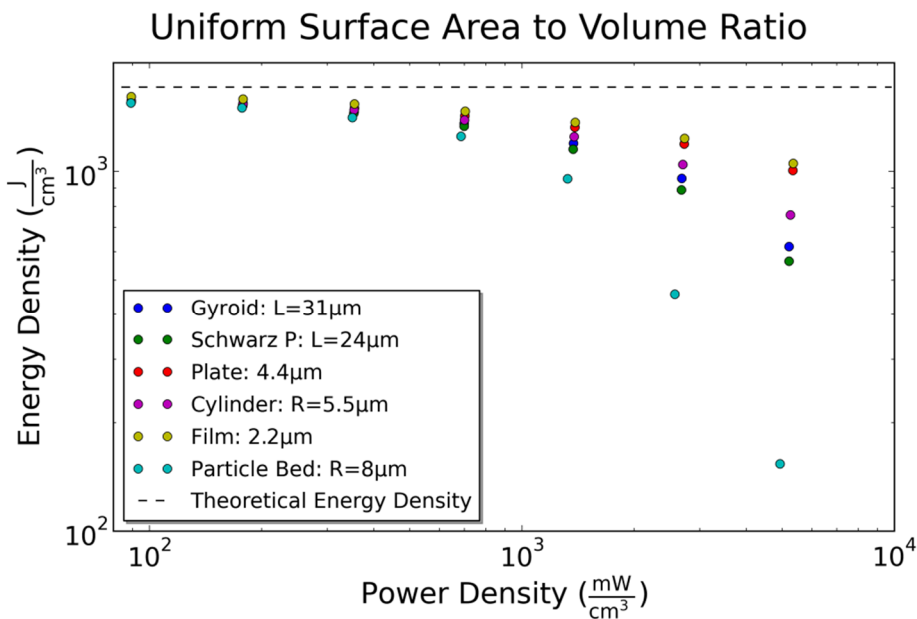


Figure 12. Comparison of all geometries with a uniform SA/V Ratio

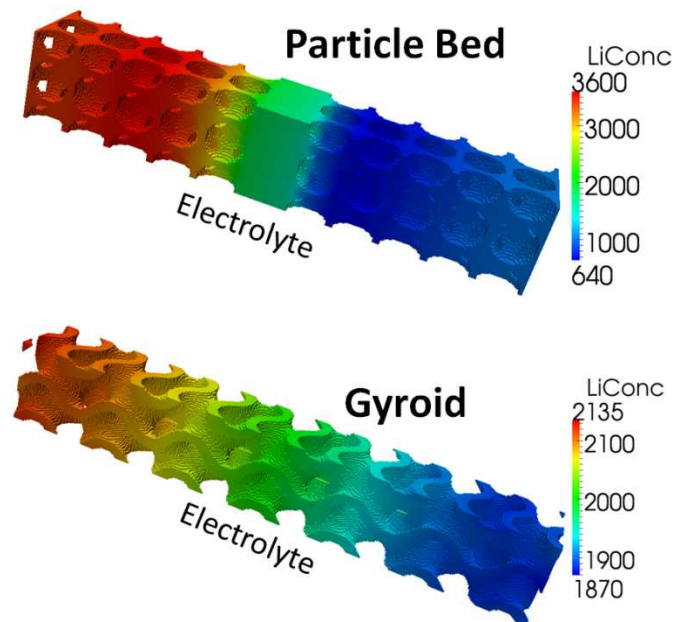


Figure 13. Lithium ion electrolyte concentration profile (mol/m³) in the particle bed battery (top) and gyroid battery (bottom). Both batteries were simulated under the same operating conditions (320 A/m² discharge current) and with comparable material volumes and electrode surface to volume ratio. The anode current collector boundary condition is applied on the left and cathode on the right.

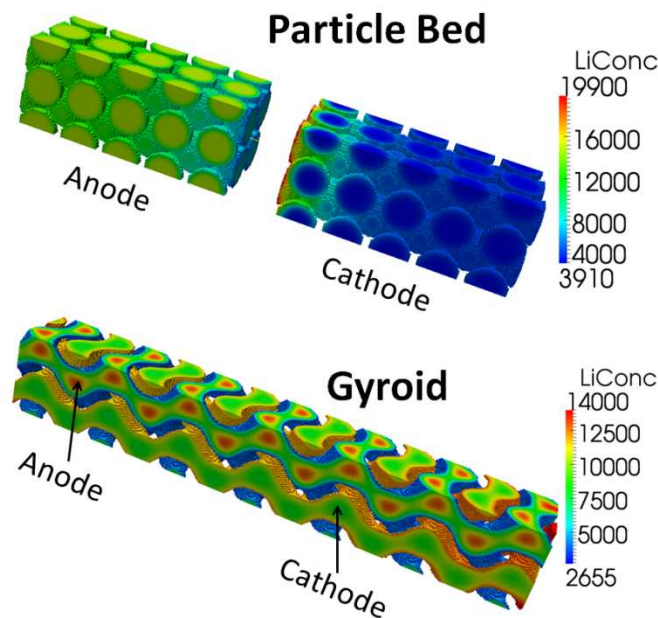


Figure 14. Lithium concentration profile (mol/m³) in the electrodes corresponding to the geometries described in Figure 13.

Uniform Minimum Electrolyte Feature Size Comparison

The previous comparison holds the SA/V ratio constant, but does not consider the resulting feature size necessary to obtain that SA/V ratio for each geometry. In reality, whichever manufacturing technique is chosen to construct a 3D microbattery will have some finite lower bound for feature resolution. A more practical comparison would be one with a uniform minimum feature size across geometries. Depending on the fabrication approach, the minimum feature size of concern may be that of the electrode or the electrolyte. Since Table 3 shows that the electrolyte contains the smallest feature in each geometry, a comparison with constant minimum electrolyte feature size, and therefore minimum overall feature size, is made here. The particle beds are manufactured using much different techniques, therefore the concept of minimum feature size is not relevant and this comparison is only across the other geometries. The battery cell width and material volume fractions are again uniform across geometries. Table 4 provides the resulting geometry characteristics associated with the comparison, and the discharge performance metrics are plotted in Figure 15.

Table 4. Geometry characteristics for uniform minimum electrolyte feature size

Geometry	Electrode Feature (μm)	Electrolyte Feature (μm)	SA/V $\times 10^{-5}$ (1 / m)	Unit Cell Size (μm)	Size Parameter
Gyroid	23.86	10	1.99	70.45 x 70.45 x 70.45	$L = 70.45 \mu\text{m}$ $t_{\text{anode}} = t_{\text{cathode}} = 0.54$
Schwarz P	16.67	10	2.06	53.3 x 53.3 x 53.3	$L = 53.3 \mu\text{m}$ $t_{\text{anode}} = t_{\text{cathode}} = 0.61$
Plate	19.13	10	1.06	58.3	
Cylinder	53.66	10	0.95	63.4 x 109.7	Radius = 26.8 μm
Film	10	10	1.00	30	

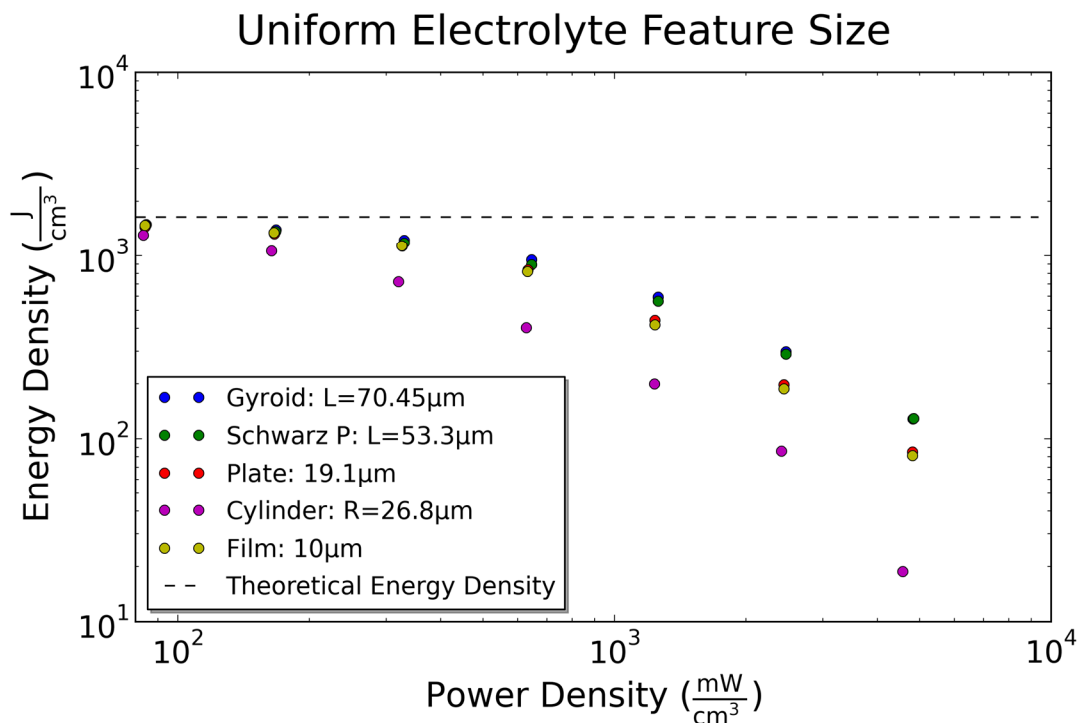


Figure 15. Comparison of electrode geometries with a uniform minimum electrolyte feature size

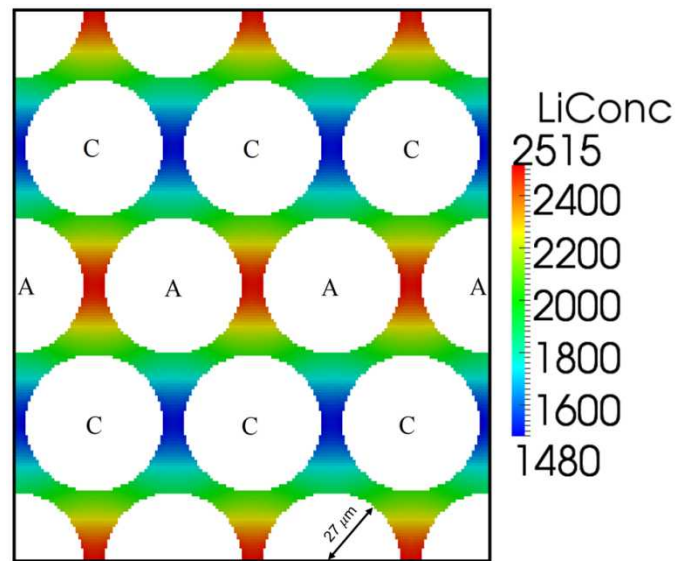


Figure 16. Electrolyte concentration profile (mol/m^3) of interdigitated cylinders geometry cross-section, taken in the middle of the battery, equidistant from the two current collector boundaries

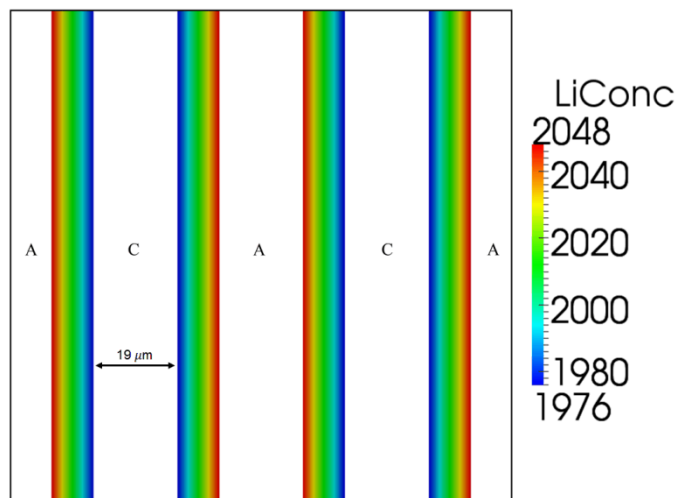


Figure 17. Electrolyte concentration profile (mol/m^3) of interdigitated plates geometry cross-section

Uniform Minimum Electrode Feature Size Comparison

If a particular manufacturing technique only required a minimum electrode feature size, then one final comparison would be useful. Battery width and material ratios are held uniform while the geometry sizes are scaled such that the minimum electrode feature size is uniform ($10 \mu\text{m}$). Table 5 provides the resulting geometry characteristics associated with the comparison, and the discharge performance metrics are plotted in Figure 18.

Table 5. Geometry characteristics for uniform minimum electrode feature size

Geometry	Electrode Feature (μm)	Electrolyte Feature (μm)	SA/V $\times 10^{-5}$ (1 / m)	Unit Cell Size (μm)	Size Parameter
Gyroid	10	4.19	4.76	29.5 x 29.5 x 29.5	$L = 29.5 \mu\text{m}$ $t_{\text{anode}} = t_{\text{cathode}} = 0.54$
Schwarz P	10	6.00	3.44	32 x 32 x 32	$L = 32 \mu\text{m}$ $t_{\text{anode}} = t_{\text{cathode}} = 0.61$
Plate	10	5.23	1.99	30.5	
Cylinder	10	1.86	5.29	11.8 x 20.5	Radius = $5 \mu\text{m}$
Film	10	10	1.00	30	

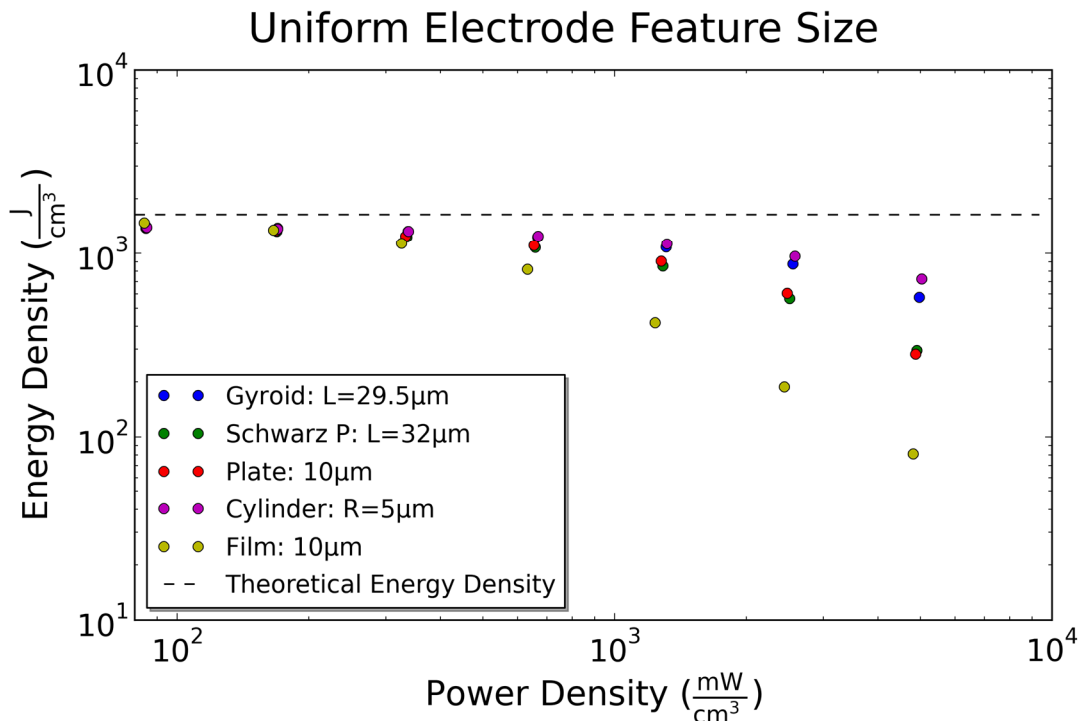


Figure 18. Comparison of electrode geometries with a uniform minimum electrode feature size

Thiele Modulus

The application of the previously defined Thiele modulus parameter is demonstrated by comparing to the uniform SA/V ratio comparison shown in Figure 12. We investigate the anode Thiele modulus ($h_{T,s}$) where the previously mentioned quantities correspond to the anode material properties and geometry characteristics, presented in Table 1 and Table 3. Similarly, the electrolyte Thiele modulus ($h_{T,e}$) is calculated for the uniform SA/V case. Both moduli are presented in Figure 19. Plotting the inverse h_T values allows us to more easily compare these results with those presented in Figure 12, since an increase in y-axis value similarly represents an increase in performance due to decreased diffusion limitations.

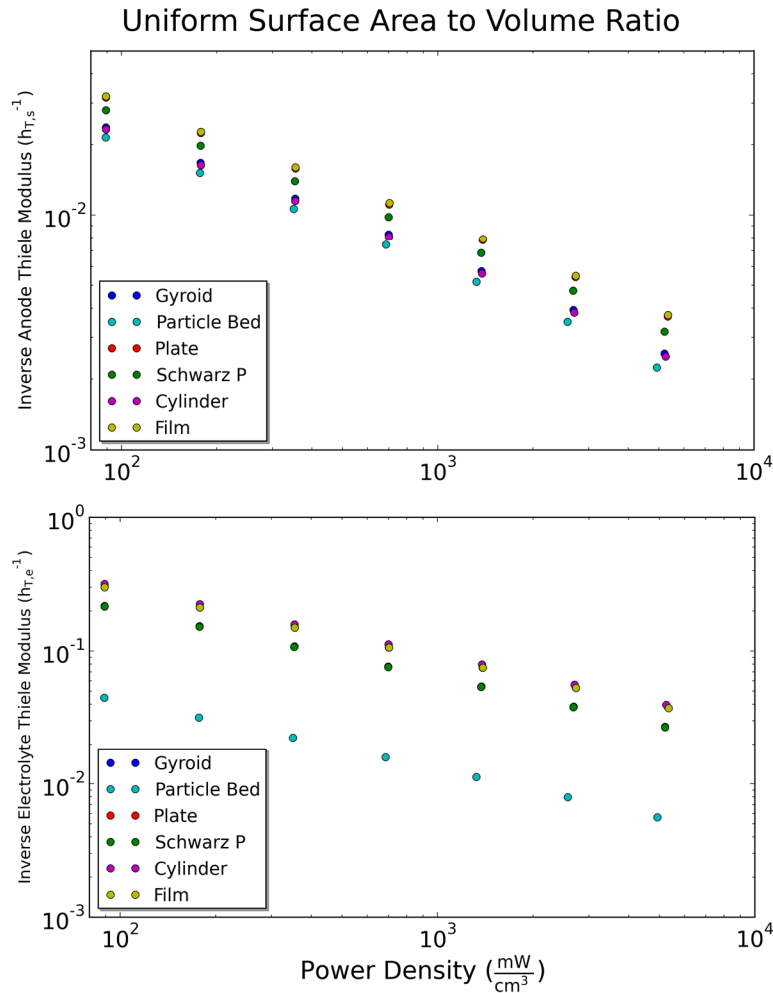


Figure 19. Plots of the inverse Thiele modulus vs. power density for both anode and electrolyte across the uniform SA/V cases previously presented

Mesh Dependence

A mesh dependency study is performed to quantify error due to physical space discretization and determine an appropriate mesh sizing for these particle-scale simulations. To be clear, we are not comparing to an analytical or exact solution, as no amount of hexahedral mesh refinement will lead to the exact representation of a curved surface. To compare mesh size effects, various discharge currents are applied to a range of meshes representing the gyroid geometry discussed above. The coarsest mesh used is composed of cubic cells with an edge length (Δx) of $2 \mu\text{m}$ ($\sim 3,400$ cells), and the finest mesh contains cubic cells with a $0.333 \mu\text{m}$ edge length ($\sim 4.4\text{M}$ cells). For this geometry, gyroid feature sizes are approximately $5\text{-}10 \mu\text{m}$. Due to the high concentration gradients formed, a higher mesh error is expected at high power densities. Figure 20 shows the dependence of error in energy density on mesh size, while Table 6 provides the data used to create the relative error vs. mesh size plot. The finest mesh shows

errors of 0.0% since those results were considered to be the exact solution for this study. We see that a $\Delta x = 1 \mu\text{m}$ cell results in only a 1-2% error, while a slightly finer mesh size of $\Delta x = 0.667 \mu\text{m}$ results in errors of less than 1% for all discharge currents. This study allows us to be confident that using finite volume cells approximately $0.667 \times 0.667 \times 0.667 \mu\text{m}^3$ in size sufficiently minimizes spatial discretization sizing error, thus it is the mesh size used throughout the previous sections.

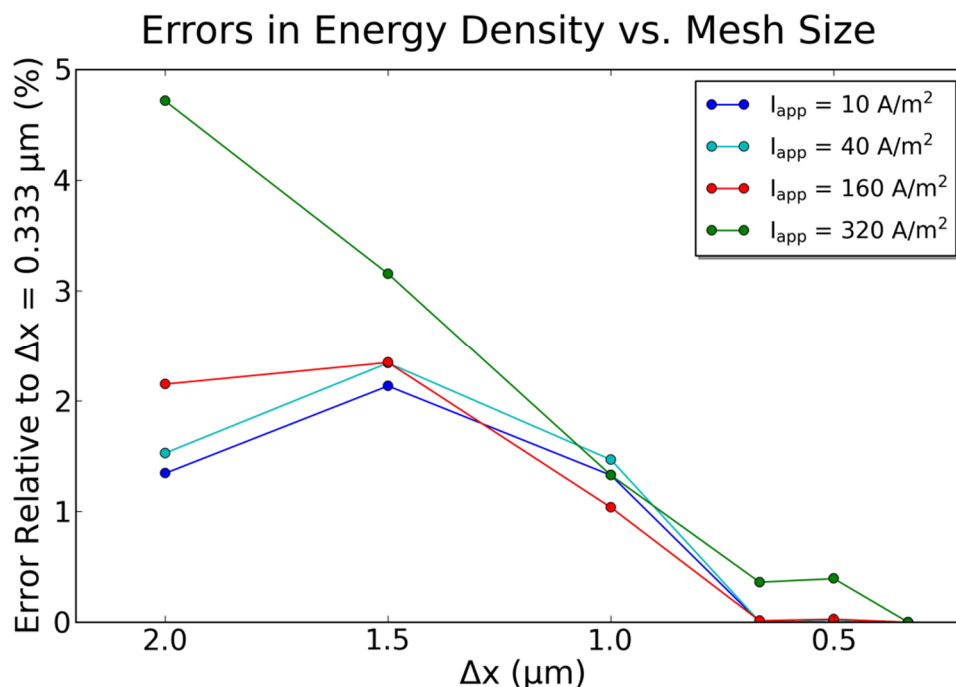


Figure 20 Errors in energy density relative to finest mesh for four discharge currents

Table 6. Relative errors in energy density for each mesh size

$\Delta x (\mu\text{m})$	Applied Current (A/m^2)			
	10	40	160	320
2.0	1.35%	1.53%	2.15%	4.72%
1.5	2.14%	2.34%	2.35%	3.16%
1.0	1.33%	1.47%	1.04%	1.33%
0.667	0.00%	0.01%	0.01%	0.36%
0.5	0.02%	0.02%	0.03%	0.39%
0.333	0.0%	0.0%	0.0%	0.0%

Comparisons Between Three-Material Volume-Averaged Model and Particle-Scale Model

In order to determine the accuracy of the volume-averaged model, we compare discharge simulation results to the particle-scale results. For simple electrode geometries such as the cylinder or plate arrays, analytically derived diffusion lengths can be used. For more complicated geometries like the gyroid or Schwarz P, an appropriate single diffusion length to

represent the entire structure is not easily defined. We investigate several methods for determining a diffusion length for such structures to enable accurate large-scale full battery simulations.

Extruded Geometries: Plate and Cylinder Arrays

Since analytical diffusion lengths can be derived for cylinder and plate-like geometries [28], we first compare the model to the particle-scale simulations of such structures. We begin with a comparison to the uniform surface area to volume ratio (SA/V) case. Table 7 contains information from the particle-scale geometry as well as the microstructural metrics required by the volume-averaged model. The SA/V ratio displayed here comes directly from the meshed particle-scale geometries and does not match theoretical values due to hexahedral (non-conformal) meshing. Diffusion length (l_d) values are calculated using the analytically derived relations presented in the previous section.

Table 7. Parameters for volume-averaged simulation of simple geometries (uniform SA/V case)

Geometry	Electrode Feature Size (μm)	Diffusion Length (l_d) (μm)	Volume Fraction (ϵ) (μm)	SA/V $\times 10^{-5}$ (m^{-1})	Specific Surface Area (a) $\times 10^{-5}$ ($\epsilon \cdot \text{SA/V}$) (m^{-1})
Plate	4.4	0.726	0.325	4.59	1.49
Cylinder	11	1.375	0.326	4.55	1.48

Figure 21 shows the Ragone plot for the particle-scale model uniform SA/V comparison. In addition, the volume-averaged results using analytically-derived diffusion lengths are plotted. As in the particle-scale simulations, the discharge rates here range from 5-320 A/m² (approximately 0.2C-25C). A visual comparison of discharge curves does not yield any additional information, as they only reflect the higher/lower energy density calculations shown here. The relative errors between the two models are presented in Figure 22.

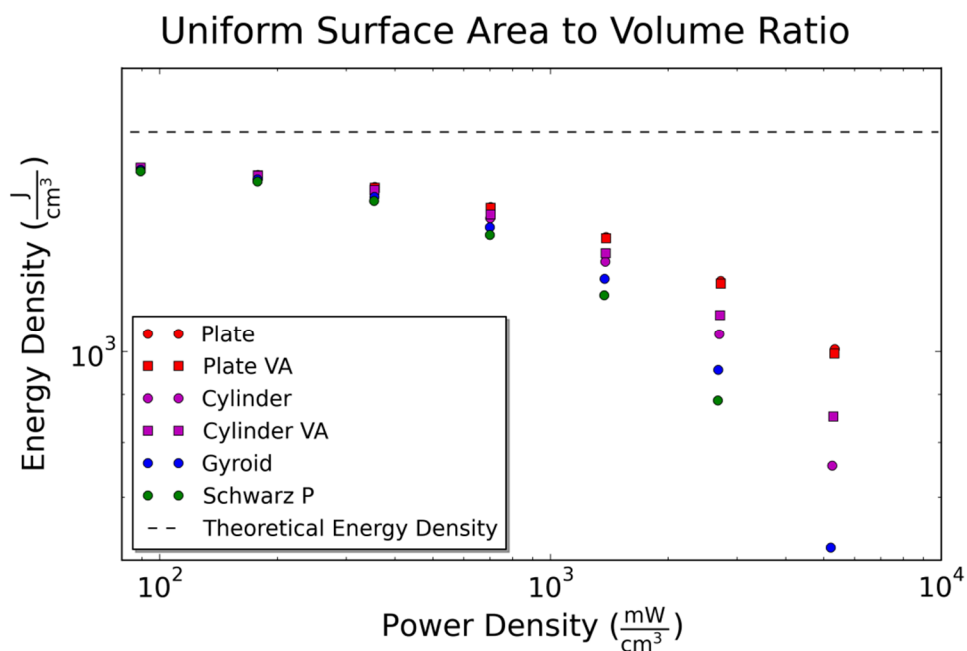


Figure 21. Ragone plot including volume-averaged results (VA) in addition to particle-scale results

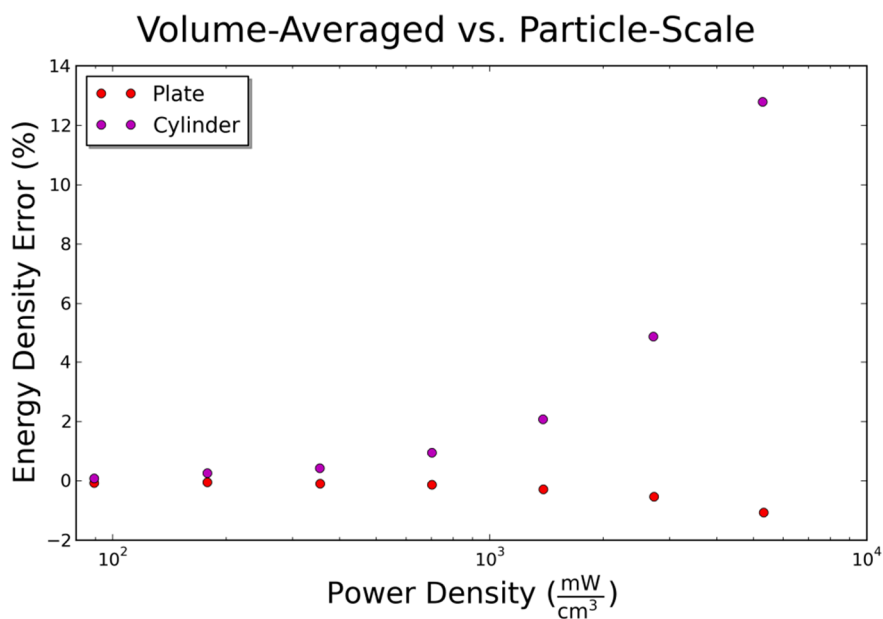


Figure 22. Errors in energy density between the volume-averaged model and particle-scale model (uniform SA/V case)

A comparison to the uniform electrolyte feature size case is made as well. Table 8 contains the microstructural summary required by the volume-averaged model with diffusion lengths once again calculated using the derived relations. For this comparison, we forgo showing the Ragone plot and plot the relative errors between the volume-averaged model and the particle-scale model in Figure 23.

Table 8. Parameters for volume-averaged simulation of simple geometries (uniform electrolyte feature size case)

Geometry	Electrode Feature Size (μm)	Diffusion Length (l_d) (μm)	Volume Fraction (ϵ) (μm)	SA/V $\times 10^{-5}$ (m^{-1})	Specific Surface Area (a) $\times 10^{-5}$ ($\epsilon \cdot \text{SA/V}$) (m^{-1})
Plate	19.13	3.156	0.325	1.06	0.345
Cylinder	53.66	6.7	0.325	0.95	0.309

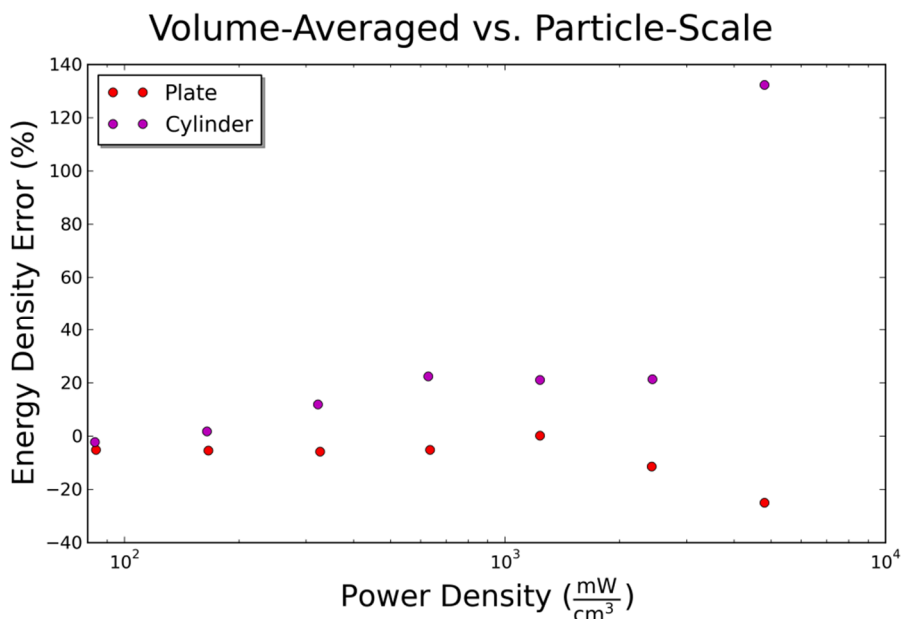


Figure 23. Errors in energy density between the volume-averaged model and particle-scale model (uniform electrolyte feature size case)

Minimal Surface Geometries: Gyroid and Schwarz P

While diffusion lengths can be easily calculated for symmetric shapes like cylinders, spheres, or plates, 3D batteries where no axis of symmetry is apparent present a more complicated scenario. Furthermore, these shapes vary in thickness throughout the battery, making the calculation of one single diffusion length difficult. In order to determine a diffusion length that most closely reflects particle-scale simulations, we investigate the error profile of a range of diffusion lengths for both the gyroid and Schwarz P geometries. As in the previous section, we first consider the uniform SA/V case. Relevant volume-averaged microstructure parameters are summarized in Table 9 and error plots similar to Figure 22 and Figure 23 are

presented for both geometries for a range of diffusion lengths in Figure 24. To maintain readability, not all diffusion lengths simulated are plotted in this figure.

Table 9. Parameters for volume-averaged simulation of minimal surface geometries (uniform SA/V case)

Geometry	Electrode Feature Size (μm)	Volume Fraction (ϵ) (μm)	SA/V $\times 10^{-5}$ (m^{-1})	Specific Surface Area (a) $\times 10^{-5}$ ($\epsilon \cdot \text{SA/V}$) (m^{-1})
Gyroid	10.5	0.325	4.53	1.47
Schwarz P	7.5	0.325	4.60	1.50

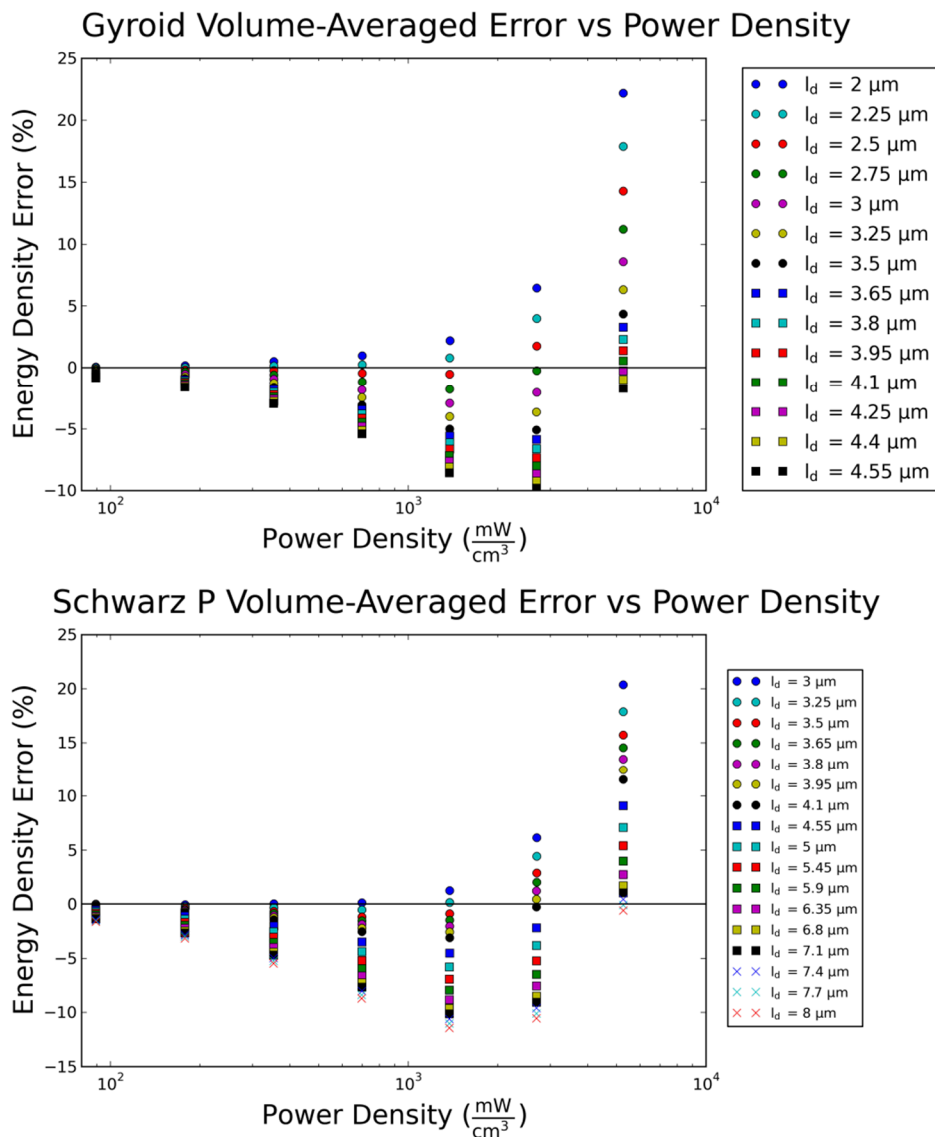


Figure 24. Error in volume-averaged energy density for both the gyroid (top) and Schwarz P (bottom) geometries for a range of diffusion lengths

Table 10. Diffusion lengths that result in the lowest observed L2-error (uniform SA/V case)

I_{app} (A/m ²) Range	Gyroid		Schwarz P	
	Min. Error l_d (μ m)	L2-error	Min. Error l_d (μ m)	L2-error
5-5	2.25	0.03	3	0.00
5-10	2.25	0.03	3	0.06
5-20	2.25	0.13	3	0.06
5-40	2.25	0.28	3	0.12
5-80	2.5	0.77	3.25	0.70
5-160	2.5	1.90	3.65	3.11
5-320	3.25	8.80	4.7	11.13

In addition to the Ragone plot, we plot the error results for each simulated discharge current as a function of diffusion length in Figure 25. We observe more clearly here that an increase in diffusion length results in a lower energy density, and that for each discharge current, there is a corresponding zero-error diffusion length. Linearly interpolated zero-error diffusion lengths for each discharge current are supplied in Table 11 and visualized in Figure 26. An exponential least squares curve fit and corresponding equation is included in the figure to allow for more convenient use of the results.

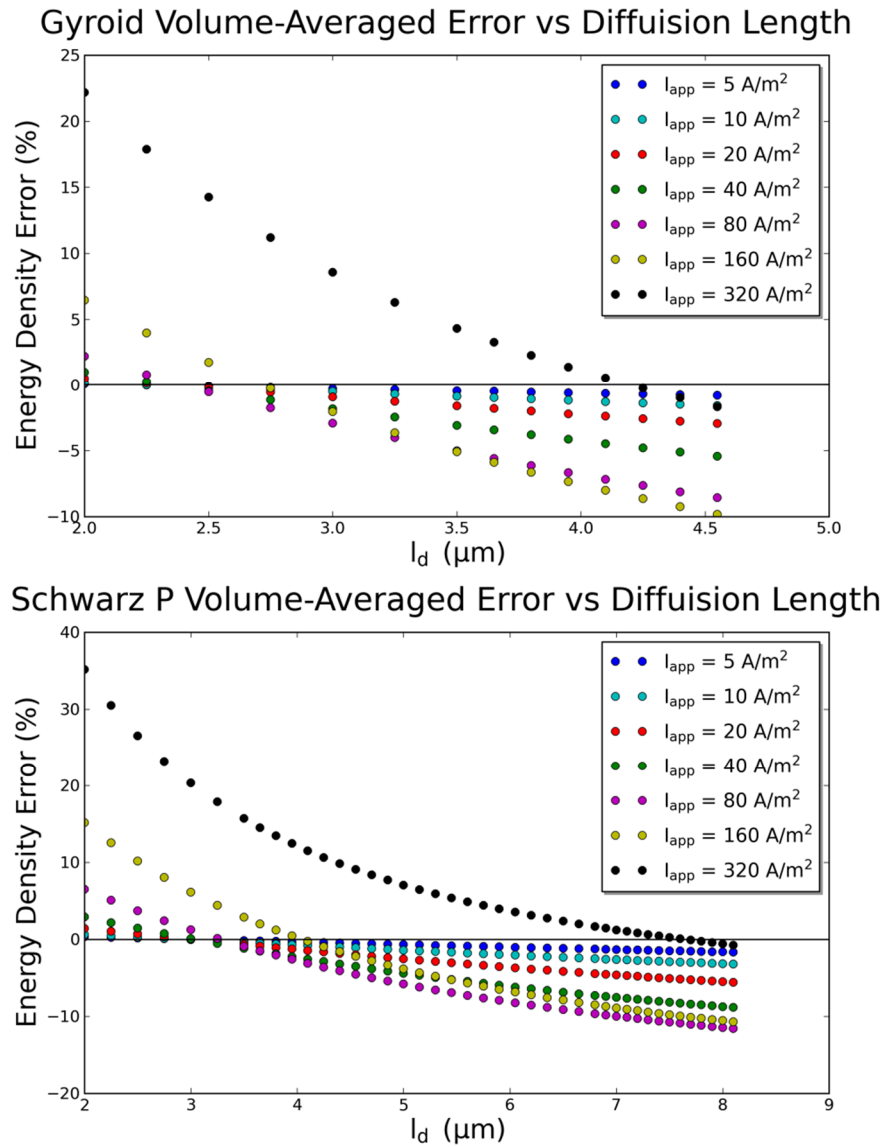


Figure 25. Volume-averaged errors in energy density vs diffusion length for both the gyroid (top) and Schwarz P (bottom) geometries (uniform SA/V case)

Table 11. Linearly interpolated zero-error diffusion lengths for each discharge current (uniform SA/V case)

$I_{app}(\text{A/m}^2)$	Gyroid l_d (μm)	Schwarz P l_d (μm)
5	2.17	3.01
10	2.25	2.91
20	2.34	3.01
40	2.34	3.04
80	2.40	3.28
160	2.72	4.04
320	4.20	7.65

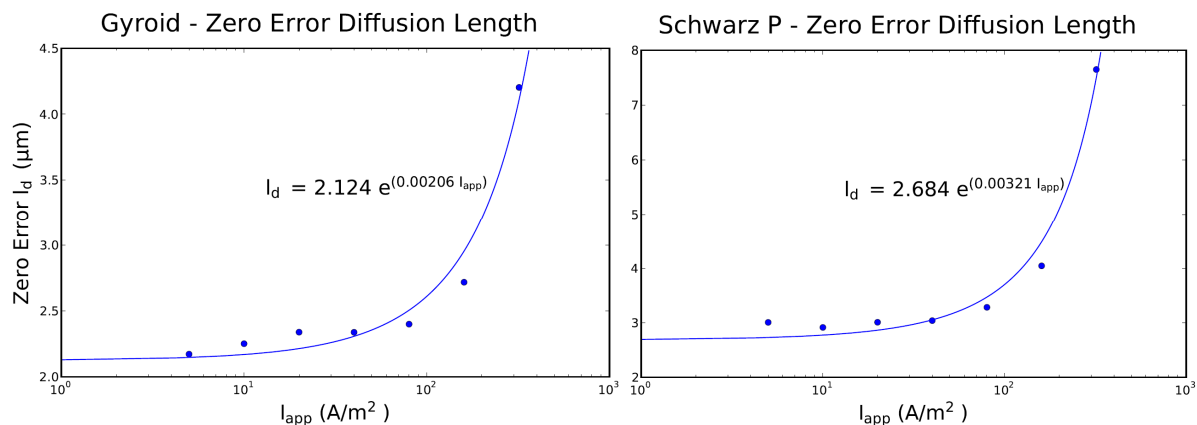


Figure 26. Zero-error diffusion lengths vs discharge current including exponential curve fits (uniform SA/V case)

A comparison to the uniform electrolyte feature size case is made for these geometries as well. Relevant geometrical information is presented in Table 12. A Ragone-like error plot similar to Figure 24 is not included here for brevity, but error- minimizing diffusion lengths for various discharge rates are likewise provided in Table 13.

Table 12. Parameters for volume-averaged simulation of minimal surface geometries (uniform electrolyte feature size case)

Geometry	Electrode Feature Size (μm)	Volume Fraction (ϵ) (μm)	SA/V $\times 10^{-5}$ (m^{-1})	Specific Surface Area (a) $\times 10^{-5}$ ($\epsilon \cdot \text{SA/V}$) (m^{-1})
Gyroid	23.86	0.326	1.99	0.649
Schwarz P	16.67	0.325	2.06	0.67

Table 13. Diffusion lengths that result in the lowest observed L2-error (uniform electrolyte feature size case)

$I_{app}(A/m^2)$ Range	Gyroid		Schwarz P	
	Min. Error l_d (μm)	L2-error	Min. Error l_d (μm)	L2-error
5-5	0	0.92	0	0.17
5-10	1.5	2.24	2.25	2.30
5-20	2.75	4.52	4.5	4.46
5-40	4.5	7.07	6	7.63
5-80	6	14.21	7.5	14.32
5-160	8	27.05	10	28.22
5-320	12	47.79	16	50.00

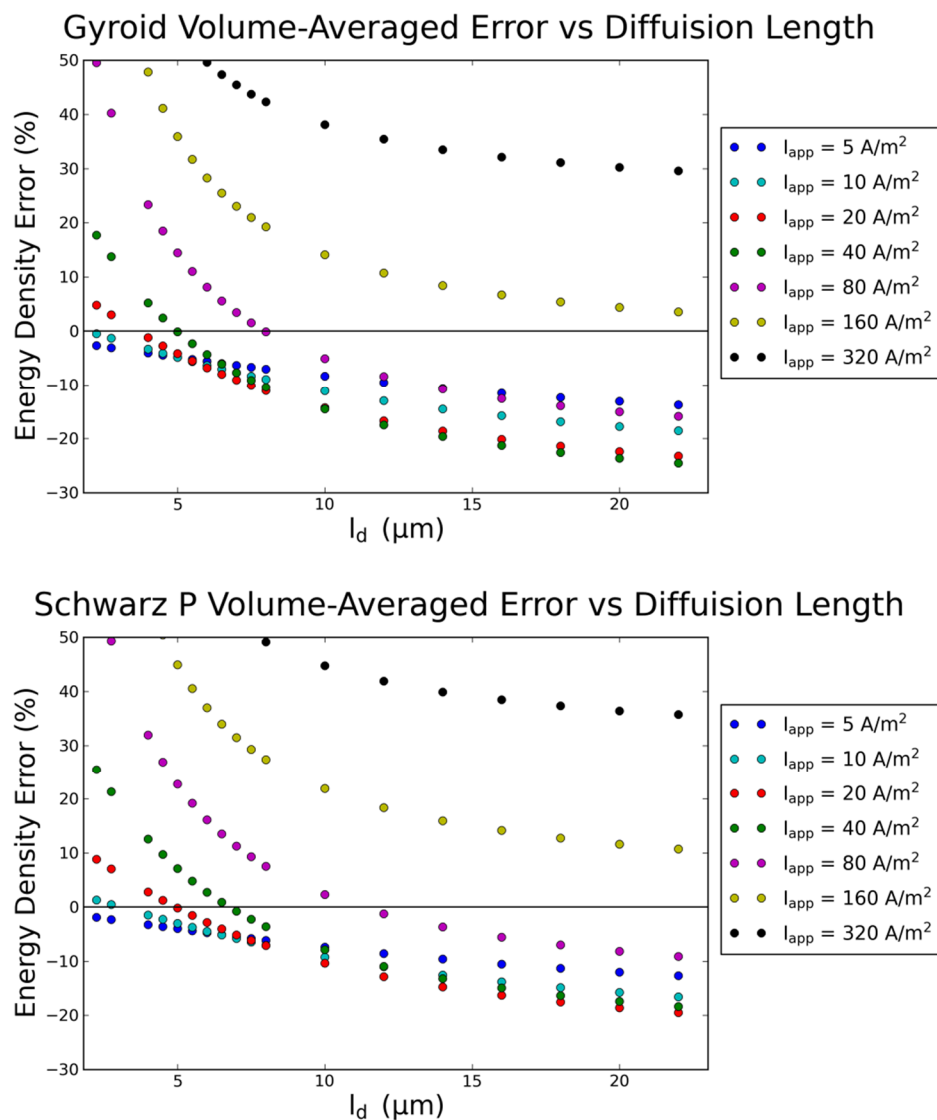


Figure 27. Volume-averaged errors in energy density vs diffusion length for both the gyroid (top) and Schwarz P (bottom) geometries (uniform electrolyte case)

Table 14. Linearly interpolated zero-error diffusion lengths for each discharge current (uniform electrolyte case)

$I_{app}(\text{A/m}^2)$	Gyroid l_d (μm)	Schwarz P l_d (μm)
5	-	-
10	1.96	3.05
20	3.65	4.93
40	4.98	6.76
80	7.96	11.30
160	-	-
320	-	-

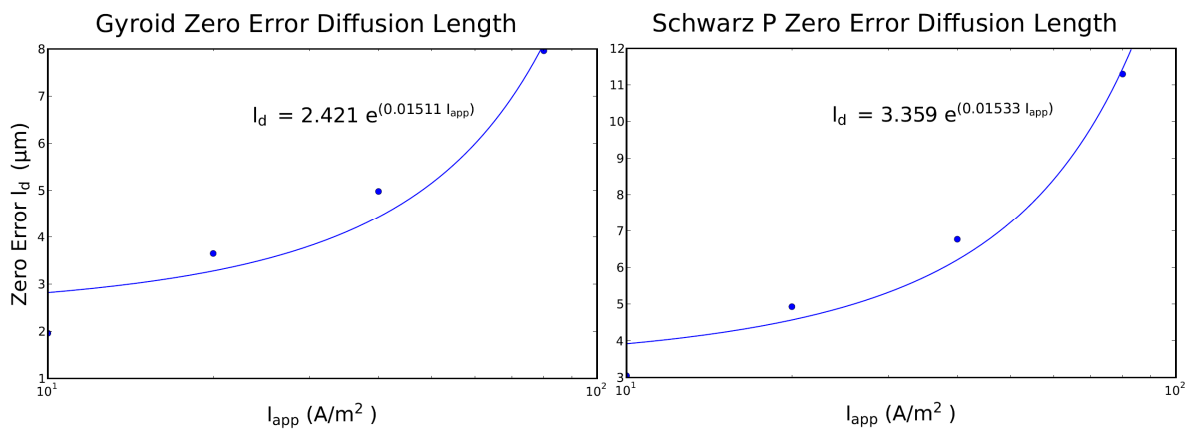


Figure 28. Zero-error diffusion lengths vs discharge current including exponential curve fits (uniform electrolyte case)

DISCUSSION:

Uniform Surface Area to Volume Ratio Comparison

The plate and film geometries provide the best energy density at high power densities. This is expected; in order to have similar SA/V ratios to the other structures, feature sizes and therefore concentration gradients are significantly smaller. Interestingly, given a similar volume fraction and SA/V ratio, the gyroid and Schwarz P structures perform similarly, perhaps due to their underlying minimal surface geometry basis.

Overall, we see significant theoretical performance improvements over a traditional particle bed battery. The particle bed geometry is outperformed by all of the other geometries, especially at high power densities where an energy density improvement of 3.7x–6.9x is observed. This improvement is attributed to the shorter ion diffusion path lengths through the electrolyte that interpenetrating structures provide when compared to the completely separated anode and cathode regions seen in the traditional particle bed geometry. To evaluate concentration profiles throughout this work, the visualization software ParaView is used [79]. Figure 13 shows the concentration profile within the electrolyte for both the particle bed and

gyroid geometries. In order to travel from anode to cathode, lithium ions must traverse a long distance in the particle bed geometry, causing a large ion concentration gradient. At a high discharge current, like the one shown in this figure, the gradient becomes such that a lithium-depleted electrolyte is seen surrounding cathode particles further from the anode. This results in a high concentration of lithium being intercalated into only the portion of the cathode closest to the anode, an effect seen in the corresponding electrode concentration profile in Figure 14. This electrolyte depletion causes a low cathode material utilization, resulting in the low energy density observed for the particle bed geometry in Figure 12. At lower discharge currents, the gradient formed in the electrolyte is not sufficient to cause significant electrolyte lithium depletion. In contrast, the gyroid structure concentration profiles in Figure 13 and Figure 14 show a more uniform electrolyte lithium ion concentration and relatively uniform electrode intercalation, even at the same high discharge rate. We see here that electrolyte diffusion becomes the limiting factor in a particle bed geometry at high discharge rates. The interpenetrating structures significantly shorten the electrolyte diffusion path while keeping electrode feature sizes comparable, thus providing the observed performance improvements.

Uniform Minimum Electrolyte Feature Size Comparison

The plot shows that for a minimum electrolyte feature size of 10 μm , the double gyroid structure provides the best energy vs. power density with the Schwarz P also performing well. Thus, if one wished to manufacture the best performing 3D battery microstructure with a minimum overall feature size, the bi-continuous triply periodic double gyroid would be the best choice. While the performance trends are not expected to be dependent on choice of electrolyte feature size (10 μm here), the magnitude or significance of better/worse performance would be expected to decrease as feature size decreases and/or applied discharge current decreases.

The SA/V ratio is an important metric for battery performance characterization or prediction. A high SA/V ratio provides more reaction area for a given amount of volume, allowing faster lithium transport between electrode and electrolyte. Table 4 shows that when material volume fractions and minimum electrolyte feature sizes are uniform across geometries, the Schwarz P and gyroid geometries have the highest SA/V ratio. In addition, the Schwarz P has the smallest electrode feature size. The combination of more surface area for transport and smaller electrode features to minimize electrode concentration gradients causes the Schwarz P geometry to perform well. However, despite a larger electrode feature size and slightly smaller SA/V ratio, the gyroid performs the best. This is likely due to the fact that the gyroid geometry has an almost uniform electrode thickness throughout its unit cell, resulting in an average electrode thickness similar to the minimum electrode thickness or feature size. In contrast, the Schwarz P has areas where the electrode is significantly thicker than its minimum thickness, resulting in a higher average electrode thickness than the gyroid.

Figure 16 depicts a cross-section of the cylinder geometry, showing electrolyte concentration values. In contrast, Figure 17 shows the concentration profile of the plate geometry cross-section, where uniform concentration values along the electrode surface are demonstrated. We see here that due to the larger feature sizes and longer path lengths through the electrolyte, the concentration gradients and concentration range are much larger in the cylinder geometry. Gradients differ by an order of magnitude within the cylinder electrolyte,

while an almost uniform gradient is present within the plate geometry electrolyte. It is likely that an improved cylinder anode/cathode orientation could decrease path lengths and gradient variability, potentially improving the poor cylinder array performance we see here.

Uniform Minimum Electrode Feature Size Comparison

Figure 18 shows that for a minimum electrode feature size of 10 μm , the interpenetrating cylinders geometry provides the best energy and power densities with the gyroid performing better than the remaining geometries.

With electrode feature sizes uniform, battery performance will depend primarily on electrolyte thickness and SA/V ratios. The packing structure of the interdigitated cylinders and material volume fraction requirements cause the electrode cylinders to be quite close to each other, resulting in a very thin electrolyte distance between them. As mentioned in the previous section and shown in Figure 16, the cylinders geometry does not fully utilize the electrolyte due to small concentration gradients in some regions, although that limitation is outweighed here by a thin electrolyte region. In addition, since the minimum feature size of the cylinder is its diameter, the entire structure has a high SA/V ratio, demonstrated in Table 5. The high SA/V ratio and thin inter-electrode distance cause the cylinders to perform the best. In order to have a similar electrode thickness, the extruded plates and films geometry SA/V ratio must decrease, causing poorer performance.

The gyroid microstructure significantly deviates from the Schwarz P structure for this set of geometry requirements. This is caused by the gyroid geometry having a higher SA/V ratio, thinner electrolyte, and smaller average electrode thickness due to the large variability in the Schwarz P shape as previously discussed. While the cylinder geometry theoretically performs the best here, it is worth noting that the gyroid geometry performs almost as well. In order to achieve an electrode feature size of 10 μm , the minimum distance between anode and cathode cylinders is 1.86 μm , while an anode to cathode separation distance of 4.2 μm results in the gyroid geometry. Although manufacturing approaches, techniques, and considerations are outside the scope of this work, it is worth noting that even if electrode feature size is the determining manufacturability factor, such a small distance between anode and cathode, less than 2 μm here, could lead to the battery short-circuiting where anode and cathode cylinders come into contact.

Thiele Modulus

In all cases the value of h_T is greater than 1, indicating that the diffusion time is greater than the reaction time, thus causing the diffusion-reaction relationship to be diffusion limited. This supports the previous discussions highlighting the effect of electrode feature size, since smaller feature thicknesses correspond to a smaller diffusion path length. While the Thiele modulus does not predict the performance magnitudes, $h_{T,s}$ does capture some performance trends, with the plate/film geometries showing the least diffusive limitation while the particles geometry shows the most. In contrast, the Schwarz P geometry is predicted to outperform the gyroid, but the opposite was true in the particle scale discharge simulations. This is likely a

result of using the minimum electrode thickness as an estimation of size for the Schwarz P structure when there are portions of the geometry that are significantly thicker than the minimum.

The relatively high mass diffusivity in the electrolyte brings the value of $h_{T,e}$ closer to a value of 1, causing $h_{T,e}$ to be an order of magnitude smaller than $h_{T,s}$. The increased electrolyte diffusion length, L_c , in the particle bed geometry accounts for its significantly higher $h_{T,e}$ value than those of the other geometries. Although we observed electrolyte diffusion limitations at high discharge rates in Figure 13, we do not observe any point where $h_{T,e} > h_{T,s}$ here. The averaged approximations made for these a priori h_T values do not account for extreme concentration variation throughout the electrode as is observed in the high discharge rate particle bed simulations. This simplified Thiele modulus calculation does appear to predict performance trends across various electrode shapes based on microstructure geometry alone and maybe a useful metric when considering electrode microstructure design.

Comparisons between Three-Material Volume-Averaged Model and Particle-Scale Model

Extruded Geometries: Plate and Cylinder Arrays

Errors for the plate geometry are quite low, staying within $\pm 2\%$ of the particle-scale results. The cylinder geometry shows more significant deviation from the particle-scale model, especially at higher discharge rates. One likely source for the error in both geometries is the assumption of a parabolic concentration profile during the derivation of a diffusion length. At very high discharge rates (the highest simulated here being 25C), a parabolic profile assumption may be inaccurate. The corrective term introduced in Equation (27) could also be less effective at high rates. A second source of error for the cylinder geometry may be in the particle-scale model implementation itself, where a hexahedral mesh is used to represent the geometry. We have acknowledged this shortcoming earlier, and here its inability to represent a curved surface may cause the theoretical diffusion length to appear less accurate. Lastly, the diffusion length of the cylinder geometry is almost double that of the plate geometry. A longer diffusion length likely also contributes to the effect of parabolic profile assumption breakdown. Overall, for these interdigitated arrays with a surface area comparable to the particle bed geometry, we see errors of less than 6% for discharge rates of up to 9C, which is a reasonable sacrifice to make when using a reduced-order model and thus gaining the ability to simulate full batteries.

Errors in the uniform electrolyte case are more significant, but remain within $\pm 22\%$ for all but the highest discharge rate. Due to the choice of electrolyte feature size for this case, electrode feature sizes, and therefore diffusion lengths, are increased $\sim 5\times$ from the previous case as demonstrated by values in Table 7 and Table 8. The same sources of error exist here as in the uniform SA/V case, but are likely exaggerated due to the larger diffusion lengths. Further studies using conformal meshes and/or using more accurate solutions to the time dependent diffusion, such as Duhamel's superposition, rather than the diffusion length method may help determine if higher volume-averaged accuracy is possible.

Minimal Surface Geometries: Gyroid and Schwarz P

Both geometries show a range of errors at each discharge rate (power density). As expected, large diffusion lengths correspond to a lower energy density, resulting in negative relative errors. At high power densities, we see a positive relative error for most diffusion lengths, indicating that the volume-averaged model is overpredicting performance at those lengths. From this group of simulations, we can determine the diffusion length that best matches the particle-scale simulation by considering the L2-norm for each length. Furthermore, we can report the diffusion length that minimizes L2 error for several ranges of simulated discharge currents, as shown in Table 10. For the entire range of discharge currents considered (5-320 A/m²), a gyroid l_d value of 3.25 μm and a Schwarz P l_d value of 4.7 μm correspond to the lowest observed L2-error. In general, L2-errors fall below 1 for all current ranges less than 80 A/m² (approx. rates of 0.2C-4C), and at these discharge rates a gyroid l_d value of 2.25 μm and a Schwarz P value of 3.0 μm are quite accurate. If we consider the electrode feature sizes, defined as the minimum electrode thickness in the domain and presented in Table 9, these l_d values correspond to roughly $R/2.33$ and $R/1.25$ for the gyroid and Schwarz P, respectively. R is considered to be the feature size half-length for consistency with the simple geometries discussed in the previous section. While an l_d value closer to the cylindrical or plate values of $R/4$ and $R/3$ might be expected, the l_d relations here are likely higher here due to the R value being based on the minimum electrode thickness for convenience and consistency with quantities of interest used in the particle-scale modeling. Figure 26 helps to demonstrate that at these feature sizes, a single diffusion length can be accurately used for discharge rates less than approximately 80 A/m² ($\sim 4C$). To summarize, if one wishes to use a single diffusion length for a range of discharge currents, the appropriate value from Table 10 should be used. For more accuracy within the rates simulated here, the exponential curve fits displayed in Figure 26 should be used.

Unlike in the uniform SA/V case, we do not see any range where a constant diffusion length yields the lowest error in the uniform electrolyte case. Due to the increased feature sizes when compared to the uniform SA/V case ($\sim 5x$ increase), it is likely that these geometries are no longer within a range that suits the diffusion length model implementation, but to get the most accurate single diffusion length within a given discharge range, Table 13 can still be used. Error plots similar in form to Figure 25 can be found in Figure 27, where significantly different behavior is observed. We see that for the lowest discharge current of 5 A/m², there is no point where the volume-averaged model overpredicts energy density, even when considering a diffusion length value of 0 μm . Conversely, there is no point where the volume-averaged energy density underpredicts the energy density for the two largest discharge currents, as they approach an asymptote at an error greater than 0. It again appears that the volume-averaged diffusion length model developed is not well-suited for such large feature sizes and/or low surface area structures. For completeness, linearly interpolated zero-error diffusion lengths are provided for discharge currents where they exist in Table 14, and again plotted along with exponential curve fits in Figure 28.

ANTICIPATED IMPACT:

The main focus of this project was to develop robust capabilities to numerically simulate lithium-ion battery particle-scale electrochemistry and utilize such capabilities to gain valuable insight into the effect of electrode microstructure on battery performance. Such capabilities are critical to capturing localized transport phenomena within an electrode particle bed and lead to a better understanding of the micro-scale geometric effects on battery performance. Such simulations also allow for better comparison with experiments, since less information is lost due to idealizations made by traditional volume-averaging modeling techniques.

This project developed a coupled numerical method to solve the governing equations for particle-scale electrochemical transport in a lithium-ion battery. The particle-scale electrochemical lithium-ion battery model is implemented within the PETSc software framework using a finite volume discretization method. The scalable implicitly-coupled implementation uses a hexahedral mesh representation of an electrode/electrolyte configuration and is used to perform discharge simulations on an array of electrode microstructures at various discharge currents. We use the model to simulate discharge performance of both traditional particle bed geometries as well as both published and novel 3D battery electrode geometries. At high power densities, we again observe diffusive limitations in the electrolyte for the particle bed geometry. From these simulations, we conclude that all of the 3D battery geometries simulated show a significant energy density performance increase over the particle bed, reaching improvements of up to 6.9x. To construct the 3D battery electrode microstructures simulated, an additive manufacturing process with a small feature size resolution is required. We therefore present a study where each geometry is required to maintain an overall minimum feature size (minimum electrolyte thickness). The double gyroid geometry performs best and both it and the Schwarz P geometry significantly outperform the less complicated interdigitated plate and cylinder 3D battery architectures. In general, the particle-scale electrochemical simulations suggest that interpenetrating 3D microbatteries outperform traditional particle bed electrodes and that a double gyroid microstructure is superior when considering the realistic manufacturing constraint of feature size resolution. Additionally, a back-of-the-envelope Thiele modulus metric is presented to approximate the performance of a 3D battery electrode geometry without performing any simulations. Applying the Thiele modulus to the geometries simulated indicates that the discharge process is diffusion limited, highlighting the importance of small electrode feature sizes in 3D microbatteries.

As a compliment to the 3D battery particle-scales simulations, a 3D battery volume-averaged model has been developed and numerically implemented using the finite volume method (FVM). The model assumes anode, cathode, and electrolyte all exist in each representative elemental volume (REV) and thus results in a system of six scalar transport equations. The equations are coupled through a surface-averaged Butler-Volmer reaction, and concentration gradients in the electrodes are approximated by the diffusion length method. By comparing to particle-scale simulations, we show that the model is quite accurate for simple geometries such as interdigitated plates and cylinders when analytically derived diffusion length relationships are used. Similarly, by simulating a range of diffusion lengths, we demonstrate that smaller minimal surface geometry batteries can be represented by a single diffusion length value. In summary, for discharge rates up to 160 A/m^2 ($\sim 9\text{C}$), we show that the 3D battery volume-

averaged model developed here can accurately simulate 3D battery electrodes that are sized to compete with particle-bed electrodes using a single diffusion length for each geometry ($<7\%$ error). Such a model makes 3D battery simulations on the full-battery scale possible without sacrificing significant accuracy.

Several 3D battery microstructures are considered in this work. This is only a small sample of possible 3D battery architectures. There are many cutting edge manufacturing techniques resulting in interesting geometries with potential for battery electrode applications. The additive manufacturing or 3D printing field is advancing quickly, and microbatteries with very small features have already been manufactured and tested [54] [53]. The PETSc implementation can be used to simulate these various geometries that were not considered for the purposes of this project. Additionally, the anode, cathode, and electrolyte materials simulated throughout this work are only one of many possible material sets that are commonly used for lithium-ion batteries [4]. Adding a material set option to our model would be a useful improvement, and would not require much effort. The only requirements to complete such a task are knowing the intrinsic properties of the materials used as well as open circuit potential curve-fits for each electrode material.

While this project did not focus on model validation, as others have compared the particle-scale model used here to experimental results [44], we would like to perform a trend comparison between the simulation capability developed here and experimental 3D microbattery studies. The model could be modified to use geometries and materials used by experimentalists to investigate the accuracy of the particle-scale model as compared to real battery discharge behavior [54] [53].

Our simulations only consider the electrochemical reactions and transport phenomena associated with lithium species and charge. In reality, there are other species present and additional chemical reactions taking place, some of which are responsible for negative battery behavior such as thermal runaway [80] [81]. This observation suggests two improvements to the current modeling presented. The first is modeling the transport and behavior of species other than lithium, and the second is to model thermal effects of battery charge/discharge. Both of these possibilities represent adding additional scalar transport equations to the governing equations as well as considering source/sink terms associated with each. Significant heat is generated at the electrode/electrolyte interface due to the reactions taking place there, and Joule heating takes place throughout the battery [82] [29].

CONCLUSION:

The particle-scale electrochemical lithium-ion battery model is implemented within the PETSc software framework using a finite volume discretization method. The scalable/parallel implicitly-coupled implementation can be run on any Cartesian grid representation of an electrode/electrolyte configuration and is used to perform discharge simulations on an array of electrode microstructures. The model is used to simulate discharge performance of both traditional particle bed geometries as well as novel interpenetrating 3D battery electrode geometries.

The simulations indicate that when a uniform surface area to volume ratio is applied across microstructures an alternating plate type of geometry provides the best performance

among the structures considered. All 3D battery designs perform significantly better than the particle bed geometry with energy density improvements of 3.7x-6.9x observed at the highest power density simulated. To construct the 3D battery electrode microstructures, an additive manufacturing process with a small feature size resolution is required. To represent this realistic constraint, each geometry is required to maintain an overall minimum feature size. The double gyroid geometry performs best and both it and the Schwarz P geometry significantly outperform the more simplistic 3D battery architectures of interdigitated plates and cylinders. Overall, the electrochemical simulations suggest that interpenetrating 3D microbatteries outperform traditional particle bed electrodes and that a double gyroid microstructure is superior when considering the realistic manufacturing constraint of feature size resolution.

A 3D battery volume-averaged model has been developed and numerically implemented in PETSc using the finite volume method (FVM). The model assumes anode, cathode, and electrolyte all exist in each REV and thus results in a system of six scalar transport equations. The equations are coupled through an interface-averaged Butler-Volmer reaction, and concentration gradients in the electrodes are approximated by the diffusion length method. By comparing to particle-scale simulations, we show that the model is quite accurate for simple geometries such as plates and cylinders when analytically derived diffusion length relationships are used. For discharge rates up to 160 A/m^2 ($\sim 9\text{C}$), relative energy density errors remain within 6% for small electrode feature sizes ($4.4\text{-}11 \mu\text{m}$) and within 22% for large electrode feature sizes ($19\text{-}54 \mu\text{m}$). Capturing particle-scale behavior of non-uniform 3D battery microstructures in a volume-averaged model is expected to be challenging. However, for smaller feature size ($7.5\text{-}10.5 \mu\text{m}$) minimal surface geometry batteries we observe that a single diffusion length value of approximately $R/2.33$ and $R/1.25$ for the gyroid and Schwarz P geometries, respectively, can be used without introducing significant error ($<7\%$) for discharge rates up to 160 A/m^2 . We observe no such consistent value for the larger feature size ($17\text{-}24 \mu\text{m}$) structures, and conclude that the limitations of the volume-averaged diffusion length model may be surpassed by these larger geometries. In summary, for discharge rates up to 160 A/m^2 ($\sim 9\text{C}$), we show that the 3D battery volume-averaged model developed here can accurately simulate 3D battery electrodes that are sized to compete with particle-bed electrodes using a single diffusion length for each geometry. Such a model makes 3D battery simulations on the full-battery scale possible without sacrificing significant accuracy.

Bibliography

- [1] M. Wakihara and O. Yamamoto, Lithium ion batteries, Wiley-VCH, 2008.
- [2] M. Armand and J. M. Tarascon, "Building better batteries," *Nature*, vol. 451, pp. 652-657, 2008.
- [3] J. Goodenough, "Oxide-ion electrolytes," *Annual review of materials research*, vol. 33, no. 1, pp. 91-128, 2003.
- [4] A. Manthiram, "Materials challenges and opportunities of lithium ion batteries," *The Journal of Physical Chemistry Letters*, vol. 2, no. 3, pp. 176-184, 2011.
- [5] J. Goodenough and Y. Kim, "Challenges for rechargeable li batteries," *Chemistry of Materials*, vol. 22, no. 3, pp. 587-603, 2009.
- [6] V. Etacheri, R. Marom, R. Elazari, G. Salitra and D. Aurbach, "Challenges in the development of advanced li-ion batteries: a review.," *Energy & Environmental Science*, vol. 4, no. 9, pp. 3243-3262, 2011.
- [7] G. Girishkumar, B. McCloskey, A. Luntz, S. Swanson and W. Wilcke, "Lithium- air battery: Promise and challenges," *The Journal of Physical Chemistry Letters*, vol. 1, no. 14, pp. 2193-2203, 2010.
- [8] P. Mukherjee, S. Pannala and J. Turner, "Modeling and simulation of battery systems," *Handbook of Battery Materials, Second Edition*, pp. 841-875, 2011.
- [9] J. Newman, K. E. Thomas, H. Hafezi and D. Wheeler, "Modeling of lithium-ion batteries," *Journal of power sources*, vol. 119, pp. 838-843, 2003.
- [10] U. Kim, C. Shin and C. Kim, "Modeling for the scale-up of a lithium-ion polymer battery," *Journal of Power Sources*, vol. 189, no. 1, pp. 841-846, 2009.
- [11] A. Manthiram, "Battery applications," *Encyclopedia of Smart Materials*, 2002.
- [12] J. Newman, *Electrochemical Systems*, Englewood Cliffs, NJ: Prentice Hall, 1991.
- [13] H. Zheng, R. Yang, G. Liu, X. Song and V. Battaglia, "Cooperation between active material, olymeric binder and conductive carbon additive in lithium ion battery cathode," *The Journal of Physical Chemistry*, vol. 116, no. 7, pp. 4875-4882, 2012.
- [14] A. Vadakkepatt and B. Trembacki, "Effective Thermal Conductivity of Lithium Ion Battery Electrodes Employing Fully Resolved Simulations for use in Volume Averaged Models," in *Summer Heat Transfer Conference*, Minneapolis, MN, 2013.
- [15] T. Drezen, N. H. Kwon, P. Bowen, I. Teerlinck, M. Isono and I. Exnar, "Effect of particle size on LiMnPO₄ cathodes," *Journal of Power Sources*, vol. 174, no. 2, pp. 949-953, 2007.
- [16] Y. H. Chen, C. W. Wang, X. Zhang and A. M. Sastry, "Porous cathode optimization for lithium cells: Ionic and electronic conductivity, capacity, and selection of materials," *Journal of Power Sources*, vol. 195, no. 9, pp. 2851-2862, 2010.
- [17] G. Liu, H. Zheng, A. Simens, A. Minor, X. Song and V. Battaglia, "Optimization of acetylene black conductive additive and pvdf composition for high-power rechargeable lithium-ion cells.," *Journal of The Electrochemical Society*, vol. 154, no. 12, pp. A1129-A1134, 2007.
- [18] H. Zheng, G. Liu, X. Song, P. Ridgway, S. Xun and V. Battaglia, "Cathode performance as a function of

- inactive material and void fractions," *Journal of The Electrochemical Society*, vol. 157, no. 10, pp. A1060-A1066, 2010.
- [19] D. Guy, B. Lestriez, R. Bouchet, V. Gaudefroy and D. Guyomard, "Novel architecture of composite electrode for optimization of lithium battery performance," *Journal of power sources*, vol. 157, no. 1, pp. 438-442, 2006.
- [20] J. S. Newman and K. E. Thomas-Alyea, *Electrochemical systems*, Hoboken, NJ: Wiley, 2004.
- [21] M. Doyle and J. Newman, "The use of mathematical modeling in the design of lithium/polymer battery systems," *Electrochimica Acta*, vol. 40, no. 13, pp. 2191-2196, 1995.
- [22] M. Doyle, T. F. Fuller and J. Newman, "Modeling of galvanostatic charge and discharge of the lithium/polymer/insertion cell," *Journal of the Electrochemical Society*, vol. 140, no. 6, pp. 1526-1533, 1993.
- [23] W. Gu and C. Y. Wang, "Thermal-electrochemical modeling of battery systems," *Journal of The Electrochemical Society*, vol. 147, no. 8, pp. 2910-2922, 2000.
- [24] P. Gomadam, J. Weidner, R. Dougal and R. White, "Mathematical modeling of lithium-ion and nickel battery systems," *Journal of Power Sources*, vol. 110, no. 2, pp. 267-284, 2002.
- [25] P. De Vidts and R. E. White, "Governing equations for transport in porous electrodes," *Journal of the Electrochemical Society*, vol. 144, no. 4, pp. 1343-1353, 1997.
- [26] J. Newman and W. Tiedemann, "Porous-electrode theory with battery applications," *AIChE Journal*, vol. 21, no. 1, pp. 25-41, 1975.
- [27] M. Doyle and J. Newman, "Comparison of Modeling Predictions with Experimental Data from Plastic Lithium Ion Cells," *J. Electrochem. Soc.*, vol. 143, no. 6, pp. 1890-1903, 1996.
- [28] C. Wang and W. Gu, "Micro-Macroscopic Coupled Modeling of Batteries and Fuel Cells," *Journal of Electrochemical Society*, vol. 145, no. 10, pp. 3407-3417, 1998.
- [29] C. Y. Wang and V. Srinivasan, "Computational battery dynamics (CBD) - electrochemical/thermal coupled modeling and multi-scale modeling," *Journal of Power Sources*, vol. 110, no. 2, pp. 364-376, 2002.
- [30] V. R. Subramanian, V. D. Diwakar and D. Tapiryal, "Efficient macro-micro scale coupled modeling of batteries," *Journal of the Electrochemical Society*, vol. 152, no. 10, pp. A2002-A2008, 2005.
- [31] V. Ramadesigan, V. Boovaragavan, J. C. Pirkle, Jr. and V. R. Subramanian, "Efficient Reformulation of Solid-Phase Diffusion in Physics-Based Lithium-Ion Battery Models," *Journal of the Electrochemical Society*, vol. 157, no. 7, pp. A854-A860, 2010.
- [32] C. Lim, B. Yan, L. Yin and L. Zhu, "Simulation of diffusion-induced stress using reconstructed electrodes particle structures generated by micro/nano-ct," *Electrochimica Acta*, 2012.
- [33] P. Shearing, L. Howard, P. Jørgensen, N. Brandon and S. Harris, "Characterization of the 3-dimensional microstructure of a graphite negative electrode from a li-ion battery," *Electrochemistry Communications*, vol. 12, no. 3, pp. 374-377, 2010.
- [34] M. Ebner, F. Geldmacher, F. Marone, M. Stampanoni and V. Wood, "X-ray tomography of porous, transition metal oxide based lithium ion battery electrodes," *Advanced Energy Materials*, vol. 3, no. 7, pp. 845-850, 2013.
- [35] V. Yufit, P. Shearing, R. Hamilton, P. Lee, M. Wu and N. Brandon, "Investigation of lithium-ion polymer battery cell failure using x-ray computed tomography," *Electrochemistry Communications*,

vol. 13, no. 6, pp. 608-610, 2011.

- [36] K. K. Bodla, J. Y. Murthy and S. V. Garimella, "Microtomography-based simulation of transport through open-cell metal foams," *Numerical Heat Transfer Part A: Applications*, vol. 58, no. 7, pp. 527-544, 2010.
- [37] J. Wilson, J. Cronin, S. Barnett and S. Harris, "Measurement of three-dimensional microstructure in a LiCoO₂ positive electrode," *Journal of Power Sources*, vol. 196, no. 7, pp. 3443-3447, 2011.
- [38] J. Joos, T. Carraro, A. Weber and E. Ivers-Tiffée, "Reconstruction of porous electrodes by fib/sem for detailed microstructure modeling," *Journal of Power Sources*, vol. 196, no. 17, pp. 7302-7307, 2011.
- [39] T. Hutzenlaub, S. Thiele, R. Zengerle and C. Ziegler, "Three-dimensional reconstruction of a LiCoO₂ li-ion battery cathode," *Electrochemical and Solid-State Letters*, vol. 15, no. 3, pp. A33-A36, 2011.
- [40] M. Ender, J. Joos, T. Carraro and E. Ivers-Tiffée, "Three-dimensional reconstruction of a composite cathode for lithium-ion cells," *Electrochemistry Communications*, vol. 13, no. 2, p. 166-168, 2011.
- [41] K. K. Bodla, J. Murthy and S. Garimella, "Direct simulation of thermal transport through sintered wick microstructures," *Journal of heat transfer*, vol. 134, no. 1, 2012.
- [42] G. Goldin, A. Colclasure, A. Wiedemann and R. Kee, "Three-dimensional particle-resolved models of li-ion batteries to assist the evaluation of empirical parameters in one-dimensional models," *Electrochimica Acta*, vol. 64, pp. 118-129, 2012.
- [43] A. H. Wiedemann, G. M. Goldin, S. A. Barnett, H. Zhu and R. J. Kee, "Effects of three-dimensional cathode microstructure on the performance of lithium-ion battery cathodes," *Electrochimica Acta*, vol. 88, pp. 580-588, 2013.
- [44] G. Less, J. Seo, S. Han, A. Sastry, J. Zausch, A. Latz, S. Schmidt, C. Wieser, D. Kehrwald and S. Fell, "Micro-scale modeling of li-ion batteries: Parameterization and validation," *Journal of The Electrochemical Society*, vol. 159, no. 6, pp. A697-A704, 2012.
- [45] P. P. Mukherjee and C.-Y. Wang, "Direct numerical simulation modeling of bilayer cathode catalyst layers in polymer electrolyte fuel cells," *Journal of the Electrochemical Society*, vol. 154, no. 11, pp. B1121-B1131, 2007.
- [46] B. Trembacki, A. Vadakkepatt, S. Mathur and J. Murthy, "A Coupled Finite Volume Method for Particle Scale Electrochemical Modeling of Lithium-ion Batteries," in *ASME 2013 IMECE Congress & Exposition*, San Diego, California, 2013.
- [47] B. Orvananos, H.-C. Yu, M. Z. Bazant and K. Thornton, "Simulations of li-ion intercalation dynamics in 3D microstructures," in *220th ECS Meeting*, Boston, MA, 2011.
- [48] S. A. Roberts, V. E. Brunini, K. N. Long and A. M. Grillet, "A Framework for Three-Dimensional Mesoscale Modeling of Anisotropic Swelling and Mechanical Deformation in Lithium-Ion Electrodes," *Journal of The Electrochemical Society*, vol. 161, no. 11, pp. F3052-F3059, 2014.
- [49] T. Hutzenlaub, S. Thiele, N. Paust, R. Spotnitz, R. Zengerle and C. Walchshofer, "Three-dimensional electrochemical Li-ion battery modelling featuring a focused ion-beam/scanning electron microscopy based three-phase reconstruction of a LiCoO₂ cathode," *Electrochimica Acta*, vol. 115, pp. 131-139, 2014.
- [50] J.-M. Tarascon and M. Armand, "Issues and challenges facing rechargeable lithium batteries," *Nature*, vol. 414, no. 6861, pp. 359-367, 2001.
- [51] J. W. Long, B. Dunn, D. R. Rolison and H. S. White, "Three-Dimensional Battery Architectures," *Chemical Reviews*, vol. 104, pp. 4463-4492, 2004.

- [52] E. B. Duoss, T. H. Weisgraber, K. Hearon, C. Zhu, W. Small IV, T. R. Metz, J. J. Vericella, H. D. Barth, J. D. Kuntz, R. S. Maxwell, C. M. Spadaccini and T. S. Wilson, "Three-Dimensional Printing of Elastomeric, Cellular Architectures with Negative Stiffness," *Advanced Functional Materials*, vol. 24, pp. 4905-4913, 2014.
- [53] J. H. Pikul, H. G. Zhang, J. Cho, P. V. Braun and W. P. King, "High-power lithium ion microbatteries from interdigitated three-dimensional bicontinuous nanoporous electrodes," *Nature communications*, vol. 4, p. 1732, 2013.
- [54] K. Sun, T.-S. Wei, B. Y. Ahn, J. Y. Seo, S. J. Dillon and J. A. Lewis, "3D Printing of Interdigitated Li-Ion Microbattery Architectures," *Advanced Materials*, vol. 25, pp. 4539-4543, 2013.
- [55] H.-S. Min, B. Y. Park, L. Taherabadi, C. Wang, Y. Yeh, R. Zaouk, M. J. Madou and B. Dunn, "Fabrication and properties of a carbon/polypyrrole three-dimensional microbattery," *Journal of Power Sources*, vol. 178, pp. 795-800, 2008.
- [56] F. Chamran, Y. Yeh, H.-S. Min, B. Dunn and C.-J. Kim, "Fabrication of High-Aspect-Ratio Electrode Arrays for Three-Dimensional Microbatteries," *Journal of Microelectromechanical Systems*, vol. 16, no. 4, pp. 844-852, 2007.
- [57] T. S. Arthur, D. J. Bates, N. Cirigliano, D. C. Johnson, P. Malati, J. M. Mosby, E. Perre, M. T. Rawls, A. L. Prieto and B. Dunn, "Three-dimensional electrodes and battery architectures," *MRS Bulletin*, vol. 36, p. 523, 2001.
- [58] L. Baggetto, R. A. H. Niessen, F. Roozeboom and P. H. L. Notten, "High Energy Density All-Solid-State Batteries: A Challenging Concept Towards 3D Integration," *Advanced Functional Materials*, vol. 18, pp. 1057-1066, 2008.
- [59] R. W. Hart, H. S. White, B. Dunn and D. R. Rolison, "3-D Microbatteries," *Electrochemistry Communications*, vol. 5, pp. 120-123, 2003.
- [60] V. Zadin, H. Kasemägi, A. Aabloo and D. Brandell, "Modelling electrode material utilization in the trench model 3D-microbattery by finite element analysis," *Journal of Power Sources*, vol. 195, pp. 6218-6224, 2010.
- [61] T. Fuller, M. Doyle and J. Newman, "Simulation and Optimization of Dual Lithium Ion Insertion Cell," *J. Electrochem. Soc.*, vol. 141, no. 1, 1994.
- [62] I. Nozad, R. G. Carbonell and S. Whitaker, "Heat conduction in multiphase systems - I: theory and experiment for two-phase systems," *Chemical Engineering Science*, vol. 40, no. 5, pp. 843-855, 1985.
- [63] V. D. Bruggeman, "Berechnung verschiedener physikalischer konstanten von heterogenen substanzen. i. dielektrizitätskonstanten und leitfähigkeiten der mischkörper aus isotropen substanzen," *Annalen der Physik*, vol. 416, no. 7, pp. 636-664, 1935.
- [64] S. V. Patankar, *Numerical Heat Transfer and Fluid Flow*, New York, NY: Taylor & Francis, 1980.
- [65] W. J. Minkowycz, E. M. Sparrow and J. Y. Murthy, *Handbook of Numerical Heat Transfer*, Wiley, John & Sons, Inc, 2006.
- [66] S. R. Mathur and J. Y. Murthy, "A Pressure-Based Method for Unstructured Meshes," *Numer. Heat Transfer B*, vol. 31, pp. 195-215, 1997.
- [67] H. S. Fogler, *Elements of Chemical Reaction Engineering*, Prentice Hall, 2005.
- [68] C. Hill, *An Introduction to Chemical Engineering and Reactor Design*, John Wiley & Sons, Inc., 1977.

- [69] S. Balay, J. Brown, K. Buschelman, V. Eijkhout, W. Gropp, D. Kaushik, M. Knepley, L. C. McInnes, B. F. Smith and H. Zhang, "PETSc users manual. Technical Report ANL-95/11 - Revision 3.3," *Argonne National Laboratory*, 2013.
- [70] S. Balay, J. Brown, K. Buschelman, V. Eijkhout, W. Gropp, D. Kaushik, M. Knepley, L. C. McInnes, B. F. Smith and H. Zhang, "Efficient Management of Parallelism in Object Oriented Numerical Software Libraries," in *Modern Software Tools in Scientific Computing*, Birkhauser Press, 1997, pp. 163-202.
- [71] HYPRE: High Performance Preconditioners, *Lawrence Livermore National Laboratory*.
<http://www.llnl.gov/CASC/hypre/>.
- [72] Texas Advanced Computing Center (TACC), *The University of Texas at Austin*.
<http://www.tacc.utexas.edu..>
- [73] CUBIT Software Version 13.0, *Sandia National Labs*. cubit.sandia.gov.
- [74] A. H. Schoen, "Infinite periodic minimal surfaces without self-intersections," *NASA Technical Note TN D-5541*, 1970.
- [75] S. Torquato, S. Hyun and A. Donev, "Multifunctional Composites: Optimizing Microstructures for Simultaneous Transport of Heat and Electricity," *Physical Review Letters*, vol. 89, no. 26, p. 266601, 2002.
- [76] M. Wohlgemuth, N. Yufa, J. Hoffman and E. L. Thomas, "Triply Periodic Bicontinuous Cubic Microdomain Morphologies by Symmetries," *Macromolecules*, vol. 34, pp. 6083-6089, 2001.
- [77] M. R. J. Scherer, *Double-Gyroid-Structured Functional Materials: Synthesis and Applications*, Springer, 2013.
- [78] D. V. Ragone, "Review of Battery Systems for Electrically Powered Vehicles," *SAE paper 680453*, 1968.
- [79] ParaView, <http://www.paraview.org/>.
- [80] T. M. Bandhauer, S. Garimella and T. F. Fuller, "A critical review of thermal issues in lithium-ion batteries," *Journal of the Electrochemical Society*, vol. 158, no. 3, pp. R1-R25, 2011.
- [81] P. Arora, R. E. White and M. Doyle, "Capacity fade mechanisms and side reactions in lithium-ion batteries," *Journal of the Electrochemical Society*, vol. 145, no. 10, pp. 3647-3667, 1998.
- [82] J. Newman, "Thermoelectric effects in electrochemical systems," *Industrial & engineering chemistry research*, vol. 34, no. 10, pp. 3208-3216, 1995.